RSC Advances

This is an *Accepted Manuscript*, which has been through the Royal Society of Chemistry peer review process and has been accepted for publication.

Accepted Manuscripts are published online shortly after acceptance, before technical editing, formatting and proof reading. Using this free service, authors can make their results available to the community, in citable form, before we publish the edited article. This *Accepted Manuscript* will be replaced by the edited, formatted and paginated article as soon as this is available.

You can find more information about *Accepted Manuscripts* in the Information for Authors.

Please note that technical editing may introduce minor changes to the text and/or graphics, which may alter content. The journal's standard Terms & Conditions and the Ethical guidelines still apply. In no event shall the Royal Society of Chemistry be held responsible for any errors or omissions in this *Accepted Manuscript* or any consequences arising from the use of any information it contains.

ROYAL SOCIETY OF CHEMISTRY

www.rsc.org/advances

Seeing is Believing: Atomic Force Microscopy Imaging For Nanomaterials Research

Jian Zhong,* Juan Yan

College of Food Science & Technology, Shanghai Ocean University, Shanghai 201306, People's Republic of China

E-mails: jzhong@shou.edu.cn; jianzhongpku@hotmail.com

RSC Advances Accepted Manuscript

Abstract: The research and development of nanotechnology have made the materials science and engineering enter the "nanomaterial era". It is pivotal to analyze the physicochemical properties of nanomaterials by developing new nanotechnological instruments. Over the past three decades, as a powerful nanotechnological imaging tool, atomic force microscopy (AFM) has provided many imaging modes for analyzing nanomaterial properties such as the topography, elasticity, adhesion, friction, electrical properties, and magnetism. The focus of this review is on the development of the AFM imaging observation for nanomaterials research. Firstly, the AFM and nanomaterials are briefly introduced. Then, AFM imaging techniques for nanomaterials research are comprehensively summarized. Finally, the advantages and disadvantages of AFM imaging techniques for nanomaterials research are discussed. This review will provide comprehensive information of AFM imaging techniques for materials scientists and engineers.

Abbreviation: LFM: lateral force microscopy; MFM: magnetic force microscopy; TRM: torsional resonance microscopy; CAFM: conductive atomic force microscopy; AFM: atomic force microscopy; STS: scanning current spectroscopy; EFM: electric force microscopy; SSPM: scanning surface potential microscopy; SCM: scanning capacitance microscopy; FMAFM: force modulation atomic force microscopy; SThM: scanning thermal microscopy; SSRM: scanning spreading resistance microscopy; STM: scanning tunneling microscopy; SEM: scanning electron microscopy; TEM: transmission electron microscopy.

RSC Advances Accepted Manuscript

1. Introduction

Atomic force microscope (AFM) is a member of the family of scanning probe microscope and was developed in 1985 as an extension of the scanning tunneling microscope by Binnig (Stanford University), Quate (Stanford University), and Gerber (IBM San Jose Research Laboratory).[1]It can be used to measure the surface properties such as morphology and mechanical properties of many materials and specimens at nanoscale level.[2-4] Moreover, it can be used to fabricate materials in a precise, controllable and reproducible fashion at nanoscale level.[5-6] Therefore, AFM is an appropriate and pivotal nanotechnology tool for nanomaterials research.

Over the past three decades, the research and development of nanotechnology have made the materials science and engineering enter the "nanomaterial era",[7-8] which created tremendous opportunities to improve basic science and engineering application. A nanomaterial is defined as a material with at least one dimension of 100 nanometers or less.[9] Compared with convetional bulk materials (e.g., materials with features in micrometer or larger size), because of surface effect, small size effect, quantum size effect, and macroscopic quantum tunnel effect, nanomaterials have numerous unique properties.[10-12] According to the chemical composition, nanomaterials can be classified into four types: (i) inorganic (e.g. quantum dots, metal nanowires and nanoceramics) nanomaterials;[13] (ii) organic (e.g. carbon nanotubes and polymer-based nanomaterials) nanomaterials;[14-15] (iii) biological (e.g. protein-based nanofibers, peptides-based nanocarriers, DNA origami) nanomaterials;[16-17] and (iv) hybridized (e.g. inorganic/organic) nanomaterials.[18] Nanomaterials have been developed to be used in wide applications such as environment,[19] energy,[20] textile engineering,[21] food,[22] disease imaging and therapy,[23] drug delivery,[24] and tissue engineering.[25] The efficacy of the nanomaterials depends on

RSC Advances Accepted Manuscript

both their physicochemical properties and their target environments. Therefore, it is important to deeply understand the properties of the nanomaterials including components, structure, surface morphology, mechanical property, etc.

In this review, the AFM and nanomaterials will be briefly introduced at first. Then, AFM imaging techniques for nanomaterials research will be comprehensively described. Finally, the advantages and disadvantages of AFM imaging for nanomaterials research will be discussed.

2. Brief Review of AFM

Since AFM was invented in 1985, AFM has become an important tool for researchers in the physical, chemical, materials, and biomedical sciences. AFM mainly uses a sharp tip, located at the end of a microscale cantilever of a probe, to sense or manipulate the samples. Then, the surface properties of the samples or pre-designed nanostructures are obtained.

AFM mainly consists of four components (Figure 1):[26] (i) An AFM probe to directly "feel" the force between the probe and a sample. An AFM probe is particularly sensitive to the interactions at the atomic level and is designed to sense them. Generally, the AFM probe has a sharp tip, typically less than 5 μm tall and often less than 10 nm in diameter at the apex, which is located at the end of a microscale cantilever, typically 100-500 μm long. (ii) A piezo scanner to precisely control the precise probe-sample position, both vertically and laterally. The piezo scanner is designed to bend, expand, and contract in a controlled, predictable manner when a voltage is applied. (iii) A professional software to control the operational parameters for controlling the probe and piezo scanner. It also can be applied to display and analyze the results. (iv) A feedback control system including a laser diode, position-sensitive photodetector, controller, a feedback circuit, and etc. The feedback

RSC Advances Accepted Manuscript

control system is applied to receive and adjust the precise probe-sample position, both vertically and laterally, by an analog/digital conversion. It is a communication system between the piezo scanner and the professional software.

An appropriate AFM probe is pivotal for the optimal performance of each AFM experiment. In AFM scanning, two kinds of major artifacts can be introduced when an AFM tip scans on the sample surface: sample height compression effect due to the elastic deformation of the sample and tip-broadening effect due to the tip-sample convolution.[27-29] There are two ways to minimize the effect of these artifacts. One is to apply surface/tip deconvolution algorithms to analyze the surface information.[30-31] The other is to choose an appropriate probe for the experiment by trying different probes. The height of the tip should be at least double the sample characterization height to prevent the contact between the cantilever and the sample.[32] Common AFM probes include silicon nitride probes, silicon probes, carbon nanotube tips, and etc.[33] Functionalized AFM probe tips can be prepared by coating polymers or proteins on the tips.[34] In addition, sphere tips can be fabricated by gluing spheres (colloid, glass, etc) to the AFM tips.[35] Except AFM probe type, the AFM performance is also dependent on the sharpness of the tip, including the radius of curvature of the tip (R_{tip}) and tip aspect ratio, and the cantilever spring constant (k).

Different AFM-based modes/methods can be used for imaging, mechanical measurements, and surface modification. According to the type of force being measured and how it is measured for AFM imaging, there are three primary AFM imaging operation modes (Table 1):[26, 36] contact mode, non-contact mode, and tapping mode. These three modes are mainly used for height imaging. Further, based on the three primary AFM imaging modes, some secondary imaging modes are developed such as deflection

RSC Advances Accepted Manuscript

imaging,[37] phase imaging,[38] lateral force imaging,[39] magnetic force gradient imaging,[40] torsional resonance imaging,[41] conductive AFM,[42] electric field gradient distribution imaging,[43] surface potential imaging,[44] electrical carrier concentration imaging,[45] force modulation imaging,[46] surface thermal imaging,[47] and scanning spreading resistance imaging.[48] Generally, the applied imaging operation mode depends on the surface characteristics of interest and the hardness/stickness of the sample. Typical surface mechanical measurements include force spectroscopy,[49] force volume,[50] nanoindentation,[51] lateral bending test,[52] two-point bending test,[53] and three-point bending test,[54] and etc. Typical surface modification methods include dip-pen nanolithography,[55-56] nanografting,[57] nanoshaving,[58] wear testing,[59] electrochemical AFM nanolithography,[60] thermal AFM nanolithography,[61] nanomanipulation,[62] and etc.

AFM can be widely applied in material science, nanoscience, medical science, biological science, semiconductor industry, and other fields. Until now, AFM has been successfully applied to image molecules on surface,[63-65] observe surface characterization,[66-69] image biological entities,[70-72] analyze material interactions,[26, 73-75], study molecular force interaction,[75-76] manipulate molecules on surface,[77-80] investigate material nanomechnics,[81-84] and mechanically fabricate 3D nanostructures.[85-89] Further, to systematically analyze the material surface properties, AFM has been explored to synergistically combine with other instruments such as the universal mechanical testing machine,[90] which can analyze the morphological changes of nanomaterials during the tensile process. In addition, AFM can also integrate with other instruments to separately obtain the morphological information and other information of the same specimens, which can help the researchers to understand the multiple properties of nanomaterials. Typical

RSC Advances Accepted Manuscript

instruments include Raman spectroscopy,[91] optical microscopy (light microscopy, epi-fluorescence microscopy, confocal laser scanning microscopy, total internal reflection fluorescence microscopy, and etc.)[92] surface plasmon resonance,[93] ellipsometry,[94] and quartz crystal microbalance.[95]

3. Imaging Observation for Nanobiomaterials Research

3.1. Height Imaging

Height imaging is a widely used application of AFM in the scientific area. It can be performed using the three primary AFM imaging operation modes: contact mode, non-contact mode (also named as frequency modulation mode), and tapping mode (also named as amplitude modulation mode or intermittant contact mode).

In contact mode, AFM tip is in physical contact with the sample surface. When the scanner gently moves the AFM tip across the sample surface (or the sample under the AFM tip), the cantilever deflection is sensitive to the change of the surface topography. During the imaging process, the cantilever deflection is maintained with the scanner movement to obtain height image. Contact mode is ideal for imaging relatively hard samples.[96] In addition, contact mode is also commonly used for high-resolution imaging.[97-98]

In non-contact mode, the cantilever is oscillated (amplitude < 10 nm) near its resonant frequency (typically 100-400 kHz). When the scanner gently moves the AFM tip across the sample surface (or the sample under the AFM tip), the tip is above the sample surface and the distance (about 1-10 nm) between the tip and the sample surface is maintained to obtain height image. The operation in this mode under ambient conditions should be careful because the water layer between the tip and the samples easily cause the tip "jump-to-contact". A high performing Z-servo feedback system and fast mechanical response of Z-

RSC Advances Accepted Manuscript

scanner are required to track the mechanical changes of the tip-sample interaction and to prevent the tip "jump-to-contact". The main advantage of non-contact mode is that the tip never contact with the sample and therefore the sample will be not disturbed or destroyed by AFM tip, which is particularly important for soft samples. Therefore, though it is not the mainstream operation mode now, many scientists are still exploring this mode for their research work.[99-100] It is commonly used for studying weakly bound-to-support samples or soft samples.

In tapping mode, the most commonly used mode, the cantilever is oscillated (amplitude > 20 nm) close to its resonance frequency (typically 100-400 kHz). When the scanner gently moves the AFM tip across the sample surface (or the sample under the AFM tip), the tip is in intermittent contact with the sample surface and the oscillation amplitude is damped. The damped cantilever oscillation amplitude is maintained to obtain height image. Tapping mode is usually used to image weakly bound-to-support samples or soft samples (polymers, DNAs, proteins, lipid bilayers, etc.). [101-104]

Height imaging can be used to analyze the morphology of the characterized nanomaterials such as nanoparticles,[105] nanotubes,[106] and nanosheets,[107-108] which is important to measure the 3D sizes of the nanomaterials and analyze the effect parameters on the nanomaterials (Figure 2).[104] Height imaging can be also applied to analyze the surface roughness of the characterized nanomaterials,[109-110] which is important to analyze and compare nanomaterials with different surface roughness (Figure 3).[111]

3.2. Deflection Imaging

Deflection imaging can be performed in contact mode AFM. In contact mode, when the tip scans on the sample surface, the tip height will be constant if the feedback system

RSC Advances Accepted Manuscript

is off. The obtained image is deflection image. This operation mode is known as constant height mode or deflection mode. It can be used to analyze the surface properties of nanomaterials by combining with height images. This mode is particularly useful for analyzing the surface properties of very flat samples in height image such as cell surface,[112] which is extremely important to analyze the effects of nanomaterials on cells. Recently, deflection imaging has been applied to observe nanodisk-like protrusions and ripples on the surface of nanosheets (Figure 4),[113] to show the 3D nanostructures of nanoparticles,[114-115] to investigate the self-assembled nanostructures of dendrimers,[116] to analyze dissolution process of nanoscrystals,[117-118] to detect the surface topography and nanostructures on the polymer thin film,[119] and etc.

3.3. Phase Imaging

Phase imaging is derived from tapping or non-contact mode.[120] In tapping or non-contact mode AFM, the cantilever is excited into resonance oscillation with a piezoelectric driver. During the AFM imaging, the oscillation of the cantilever is changed due to the tip-sample interactions. Phase imaging is the mapping of the difference between the measure phase of the cantilever's periodic oscillations and the phase of the periodic signal by the piezoelectric driver to drives the cantilever. Phase imaging shows the sample surface properties that can cause the phase shift. These sample surface properties include composition, elasticity, adhesion, friction, electrical properties, magnetism, and etc. Therefore, phase imaging mode can give valuable information of sample surface, especially when height images show no obvious difference.

Phase imaging has already been widely applied for nanomaterials research including surface composition studies of polymers by ion modification,[121-122] compositional

RSC Advances Accepted Manuscript

difference on the heterogeneous nanostructure surface,[123] quantitative characterization of phase separation in polymer-blended films,[124] and etc. For example, Jian Zhong et al.[125] used AFM to observe self-assembly process of regenerated silk fibroin from random coil nanostructures to antiparallel β-sheet nanostructures (Figure 5). The AFM height and phase images showed the height and phase periodic intervals of silk fibroin protofibrils disappeared in turn at day 1 and day 14, respectively. This work demonstrated that phase imaging can assist height imaging to analyze the detailed information of protein self-assembly process.

3.4. Lateral Force Imaging

Lateral force imaging is performed by lateral force microscopy (LFM),[126] which is also named as friction force microscopy,[127-128] to map the relative differences in the friction force between the tip and the sample surface. LFM can simultaneously obtain the height image and lateral force image. LFM is similar to contact mode AFM. In contact mode AFM, the scanning is parallel to the long axis of the cantilever, the force between the tip and the sample surface causes that the cantilever is vertically deflected, and its vertical deflection is maintained to obtain the surface property information. While in LFM, the scanning is perpendicular to the long axis of the cantilever, the force between the tip and the sample surface causes the cantilever is twisted around its long axis, and its lateral deflection is maintained to obtain the surface property information. The cantilever twisting can be resulted from the changes in surface properties (hydrophilicity, hardness, etc) or the changes in topography. By comparing the trace LFM image, the retrace LFM image, and the corresponding height image (trace or retrace image), the reason for the cantilever twisting can be distinguished.

RSC Advances Accepted Manuscript

LFM is now widely used to characterize the surface friction differences of nanomaterials, and then to analyze the composition and structural differences of nanomaterials. Pandey et al.[129] used LFM to study self-assembled layers of cyclodextrin-thiocholesterol inclusion complexes on gold (Figure 6). Height images showed no obvious height differences and LFM images showed obvious phase separation, which demonstrated that LFM has obvious advantage for analyzing self-assembled layers composed of multiple substances. LFM was also used to differentiate different phases of hydated cement paste (calcium-silicate-hydrate particles, calcium hydroxide crystals, unhydrated particles) at nanoscle and microscale.[130-131] Almeida et al.[132] used LFM to identify graphene nanosheets crystallographic orientation. The results revealed the periodicity of the graphene hexagonal structure allowed the observation of the lattice symmetries and determination of the crystal orientation. Liao et al.[133] used LFM to analyze the temperature effect on lateral force signal of the 16-mercaptohexadecanoic acid self-assembled monolayers. The LFM signal decreased with the increase of temperature, and therefore, LFM can be used to analyze the thermodynamic properties of nanomaterials.

3.5. Magnetic Force Gradient Imaging

Magnetic force gradient is imaged by magnetic force microscopy (MFM),[134] which is derived from Tapping mode. By using a sharp magnetized tip to scan a magnetic sample, the tip-sample magnetic interactions are detected to map the magnetic force gradient while the tip is above the sample surface (no touching). During MFM measurements, there are two forces between the tip and the sample surface: magnetic and Van der Waals force. Therefore, by “force range” technique or “two pass” technique, MFM can simultaneously measure height image and magnetic force gradient image.

RSC Advances Accepted Manuscript

MFM has become a well-established veritable work horse in the research field and industry field of magnetic nanomaterials-related works. Li et al.[135] characterize the mechanically exfoliated single- and few-layer MoS_2 and graphene (Figure 7) nanosheets using MFM. By analyzing the phase and amplitude shifts, it is found that magnetic response of these nanosheets depended on their layer number. Interesting, MoS_2 and graphene nanosheets became nonmagnetic when they exceeded a certain thickness. The application of MFM opens a new way to understand the intrinsic properties of 2D nanomaterials. In addition, MFM has also been applied to study magnetic nanoparticles (iron oxide nanoparticles,[136] Cu-coated iron nanoparticles,[137] magnetite nanoparticles[138]), patterned magnetic nanodots,[139] nanowires and nanotubes,[140] other magnetic nanostructures (iron nanostructures,[141] dicobalt octacarbonyl nanostructures[142]), and etc.

3.6. Torsional Resonance Imaging

Torsional resonance imaging, which is performed by torsional resonance microscopy (TRM), measures and controls dynamic lateral forces between the tip and the sample surface.[143-144] In TRM, the cantilever oscillates around its long axis in a twisting motion, which causes that the tip vibrates in a dithering motion. When the tip scan the sample surface, the vertical deflection and lateral twist of the cantilever can be simultaneously measured, and therefore, TRM can examine the in-plane mechanical properties of nanomaterials such as friction, shear stiffness, and other tribologically relevant properties.[143, 145] In addition, it can explore the complementary lateral and vertical characterization with high sensitivity by being interleaved with tapping mode.[146] TRM can provide higher resolution, sensitivity, and stability than many other imaging mode AFM. Hwang et al.[147] used TRM to image polystyrene nanosphere, DNA (Figure 8) and purple

RSC Advances Accepted Manuscript

membrane in water. The results demonstrated that TRM can provide high resolution images even when a relatively blunt tip is used. Moreover, compared with conventional non-contact mode AFM, TRM showed a higher sensitivity and stability in water, which proved that TRM can be important for analyzing soft matters in liquid and liquid-solid interfaces. Torsional resonance has also been widely used for imaging nanostructures of materials such as human hair,[41] mineral pennine,[148] protein-DNA complex,[149] and polymers.[150]

Currently, TRM is still in the developing phase. Many scientists are working on the instrument development to broaden its applications. Yang et al.[151] designed a torsional excitation system through the Lorentz force actuation for triangular-shaped and rectangular-shaped cantilevers to image nanomaterials in buffer solutions with small loading forces. The results showed the Lorentz force actuation can successfully excite different AFM cantilevers to execute pure torsional resonances in air and liquid. It showed a high force sensitivity, a high resolution, and a high stability to observe hydration layers and nanomaterials at liquid-solid interfaces. Kaidatzis et al.[152] employed torsional resonance mode in magnetic force microscopy. The results showed it had two obvious advantages over conventional magnetic force microscopy: the ability to perform magnetic force imaging without topography-related interference and the improvement (15%) of the lateral resolution. These works can broaden AFM's application for nanomaterials.

3.7. Conductive AFM

Conductive AFM (CAFM) is a powerful current sensing mode and is derived from contact mode AFM.[153] In CAFM, a DC bias is applied between a conductive tip and the sample (conducting or semiconducting sample) when the tip scans on the sample surface. CAFM can simultaneously measure the height image and current distribution imaging. The

RSC Advances Accepted Manuscript

cantilever deflection feedback signal is used to obtain a contact mode height image. The current passing between the tip and the sample is recorded to characterize conductivity variations of the nanomaterials. It can measure the current in the range of hundreds of femotoamps to nearly a microamp. CAFM is different to scanning tunneling microscopy (STM) although they both apply a DC bias between a conductive tip and the sample. STM is based on a concept of quantum tunneling. When a conductive tip is near (above) the sample surface, the DC bias allow electrons to tunnel through the vaccum. The resulting tunneling current is an exponential function of tip position, applied voltage, and the local density of states of the sample.[154] The change of the tunneling current or the height of the tip can be mapped above the sample surface by maintaining the height of the tip or the tunneling current, respectively. Therefore, the surface information of nanomaterials at an atomic level is obtained by STM.

CAFM is useful for the research of surface characterization of conducting and semiconducting nanomaterials. It has been used to show the current distribution image of nanomaterials such as GaN nanowires,[155] HgTe nanowires,[156] silicon nanowires,[157] sultrathin Al_2O_3 films,[158] SnO_2 nanobelt,[159] GeSi quantum nanorings,[160] carbon nanowalls,[161] ZnO nanorods,[162] and gold nanoparticles.[163] CAFM has also been used to show the resistance image of nanomaterials such as epitaxial graphene,[164] $LaAlO_3/SrTiO_3$ heterostructures,[165] carbon nanotube thin-film transistors,[166] and oxide layer nanostructures.[167]

Recently, based on CAFM, scanning current spectroscopy (STS) was developed for nanomaterials research. Gordon et al.[168] used STS to map current spectroscopy of heterojunctions of a molecular semiconductor (copper phthalocyanine, CuPc) and a

RSC Advances Accepted Manuscript

transparent conducting oxide (indium-tin oxide, ITO), on 20-500 nm length scales (Figure 9). Current spectroscopy maps were generated for CuPc/ITO heterojunctions as a function of ITO activation procedures and modification with variable chain length of alkyl-phosphonic acids. This work proved CAFM-based STS is a new, simple and convenient way to map the electrical property heterogeneity of transparent conductive oxide/organic semiconductor interfaces at nanometer length scales. In addition, STS has been applied to for nanomaterials research such as graphene,[169-170] and poly(3-hexylthiophene) thin films.[171]

3.8. Electric Field Gradient Distribution Imaging

Electric field gradient distribution is imaged by electric force microscopy (EFM, also named as electrostatic force microscopy),[172] which is derived from Tapping mode. In EFM, a voltage is applied between the tip and the sample while the tip is above the sample surface (no touching). In a typical EFM image, the phase, frequency, or amplitude of the cantilever oscillation is plotted versus the in-plane coordinates (X and Y). The phase, frequency, or amplitude is related to the vertical and near-vertical electric field gradient between the tip and the sample. There are two forces between the tip and the sample surface: electrostatic force and Van der Waals force. Therefore, EFM is designed to separately measures height image and electric force gradient image by “force range” technique or “two pass” technique.

EFM can be applied for analyzing the surface electrical properties of nanomaterials. Gaikwad et al.[173] used it to measure surface charge of asphaltene nanoaggregates (Figure 10). The experimental data was used to calculate the average surface charge density of the nanoaggregates as 43.7 nC/cm^2. The surface charges were dependent on the native charge of asphaltene and the solvents. In addition, EFM has also been applied to study

RSC Advances Accepted Manuscript

nanomaterials such as poly(lactic acid) nanofibers,[174] purple membranes,[175] reduced graphene oxide,[176] and polymer-carbon nanotube.[174]

3.9. Surface Potential Imaging

Surface potential is imaged by scanning surface potential microscopy (SSPM, sometimes referred to as scanning kelvin probe microscopy), which is derived from Tapping mode. It characterizes the electrostatic potential on the sample surface with or without a voltage applied to the sample. It is a nulling technique. During the imaging process, the cantilever experience a force wherever the potential on the surface is different from the potential of the tip. To nullify the force, the voltage is adjusted to make sure that the potential of the tip has the same potential to the sample surface region underneath it. Then, the surface potential image is obtained by plotting the voltage applied to the tip versus the in-plane coordinates.

SSPM has been widely used for nanomaterials research. Chen et al.[177] used SSPM to directly image the surface potential depth profile over the cross-sections of nanoscale organic photovoltaic devices as solar cells (Figure 11). They developed a bias compensation method for quantitative measurement of energy-level differences in the devices according to the measured energy band alignments using SSPM. It may provide a general method for thin-film devices to understand the mechanisms in and improvements of these devices. SSPM has also been applied to many other nanodevices (CdTe/CdS solar cells,[178] organic field-effect transistors,[179] single crystal solar cells,[180] epitaxial graphene devices,[181] CZTSSe solar cells,[182] and etc.), hybrid nanocomposites (nanoparticles/polymer hybrid blends,[183] Au nanoparticle on TiO_2 nanotubes,[184] Silver-TiO_2,[185] and etc.), ZnO nanowires,[186] graphene,[187-189] MoS_2 nanoflakes,[190] ZnO nanorods,[191] and etc.

RSC Advances Accepted Manuscript

3.10. Electrical Carrier Concentration Imaging

Electrical carrier concentration is imaged by scanning capacitance microscopy (SCM),[192] which is derived from contact mode AFM. SCM uses an ultra-sharp conductive tip (Pt/Ir or Co/Cr metal coated etched silicon tip) to form a metal-insulator-semiconductor capacitor with a semiconductor sample having an oxide layer. When the tip scans across the sample surface, a high-frequency AC bias is applied to the tip and the sample. Electrical carriers are accumulated and depleted within the surface layers, which changes the tip-sample capacitance. The capacitance changes are a function of the majority carrier concentration in semiconductors. By maintaining a constant force between the tip and the sample, both height image and surface capacitance image can be simultaneously obtained, which enables the direct correlation of local topography with electrical properties. The relative carrier concentration can be measured in the range of 10^{16}-10^{21} cm^{-3}.

Bussmann et al.[193] used SCM to image buried delta-doped donor nanostructures fabricated in Si (Figure 12). The results showed this technique could detect buried nanostructures in thin films that were flat in AFM height image, which proved SCM is a useful method for mapping the dopant profile in semiconductor devices without obvious height difference in topographical image. Some other typical applications of this technique include mapping the dopant profile in silicon nanowires,[194] interfacial abruptness analysis in heterostructures in nanowires,[195] quantification of dielectric constants of colloidal nanocrystals,[196] studies of electronic properties and size distributions of ErAs nanoparticles embedded in GaAs pn junctions,[197] analysis of memory properties and charge effect in Si nanocrystals,[198] and etc.

3.11. Scanning Spreading Resistance Imaging

RSC Advances Accepted Manuscript

Scanning spreading resistance is imaged by scanning spreading resistance microscopy (SSRM),[199] which is derived from contact mode AFM. During the imaging process, a DC bias is applied between a conductive tip and the sample. The resulting current between the tip and the sample is measured to map the local spreading resistance.

SSRM has already been widely used for nanomaterials research including quantitative 2D-carrier distribution of nanowire-based transistors [200] and metal-oxide-silicon field effect transistor,[201] surface resistance observation of multi-walled carbon nanotube-polymer nanocomposites[202] and TiN/HfO_2-based resistive switching structures,[203] Quantitative 3D carrier mapping of nanowire-based transistors,[204] device failure analysis of polycrystalline silicon gate originated complementary metal oxide semiconductor,[205] compositional contrast analysis in nanoheterostructures,[206] nanoscale electronic properties analysis of CdZnTe crystals,[207] and etc. For example, Truchly et al.[208] used SSRM to analyze the electronic properties of $YBa_2Cu_3O_{6+x}$ thin films. Before the ion beam etching, the SSRM image (Figure 13b) showed that the thin film surface conductivity was very low and only some current flows through the highest surface irregularities in AFM height image (Figure 13a). Further, they removed the degraded surface layers of the thin film by ion beam etching and observed the surface by SSRM. The results showed a high inhomogeneity on micrometer and nanometer scale with numerous regions of highly enhanced conductivity compared to the surroundings.

3.12. Force Modulation Imaging

Force modulation imaging is performed by force modulation AFM (FMAFM), which is derived from contact mode AFM. It is designed to analyze and map the differences in surface stiffness or elasticity of a sample.[209] It allows simultaneously obtain both height image and force modulation image. During the imaging process, the tip tracks the sample

RSC Advances Accepted Manuscript

topography (height image) as in normal contact mode. In addition, a periodic mechanical signal (typically less than 5 kHz) is applied to the base of the cantilever and the cantilever moves with a small vertical oscillation (modulation) which is significantly faster than the AFM x-y raster scan rate. The force on the sample is modulated such that the average force on the sample is equal to that in contact mode. A stiff sample surface deforms the oscillation less than a soft surface. Therefore, the variation in cantilever deflection amplitude at the frequency of modulation is related with the relative stiffness/elasticity of the surface.

FMAFM can be applied for nanomaterials research including the characterization of polymer blends,[210] analysis of polymer interdiffusion in carboxylated nanolatices,[211] observation of semiconductor nanoheterostructures,[212] observation of nanostructures in single crystals,[213] and etc. For example, Zhao et al.[214] used FMAFM to characterize the local mechanical properties of the interphase region of epoxy matrix reinforced by carbon fibers with or without the grafting of polyhedral oligo silsesquioxane/carbon nanotubes (Figure 14). The force modulation images and section analysis images showed obvious contrast among the carbon fiber, interphase, and matrix region. The presence of polyhedral oligo silsesquioxane/carbon nanotubes induced a distinct and slow modulus transition region corresponding to the interphase.

3.13. Surface Thermal Imaging

Surface thermal is imaged by scanning thermal microscopy (SThM),[215-216] which is derived from contact mode AFM. As with many other modes, SThM can simultaneously acquisite both height image and surface thermal image. During the imaging process, a

RSC Advances Accepted Manuscript

temperature-sensitive tip is applied to scan the sample surface and then the local temperature and thermal conductivity of the sample surface is mapped.

SThM is mainly applied to analyze the surface temperature-related properties of nanomaterials such as thermal imaging of individual silicon nanowires,[217] thermal conductivity measurements of silicon/germanium nanowires[218] and graphene,[219] quantitative temperature measurement of an electrically heated carbon nanotube,[220] correlation study between thermal properties and morphology of thin films,[221] and direct electrocaloric measurements of a multilayer capacitor.[222] For example, Grauby et al.[218] used SThM to observe the thermal image of silicon/germanium nanowires (Figure 15). The local conductance increases when the heat flux is directly applied on a nanowire. The statistical distribution of the voltage signal on the thermal image was summarized for further thermal conductivity calculation.

4. Summary and Outlook

To sum up, the review summarized the application of AFM imaging for nanomaterials research. As a powerful nanotechnological imaging tool, AFM will undoubtedly attract the attention of more and more materials scientists and engineers in the future. Compared with other nanotechnological microscopic techniquese such as SEM and transmission electron microscopy (TEM), AFM has many advantages for nanomaterials investigations. (i): AFM can provide a true three-dimensional surface profile of nanomaterials such as graphene[223] and carbon nanotube[224], which will be useful for analyzing nanomaterial morphology, the height of the materials of interest and surface roughness of nanomaterials. (ii): AFM has high spatial resolution (Z direction: sub-nanometer scale; X-Y direction: nanometer scale) for nanomaterials characterization.[225] (iii): The sample preparation of AFM samples is

RSC Advances Accepted Manuscript

simple and easy. Negative staining pretreatment is needed for TEM observation of biological samples.[226] Gold sputtering pretreatment is needed for SEM observation of non-conductive samples.[227] No complicated preparations or chemical modifications were required for AFM samples. (iv): the samples can be detected in various environments (atmosphere, liquid, vacuum, cryo) by AFM.[228-229] In particular, AFM can be applied to in situ observe the materials interactions in a liquid environment, such as the interactions between biomolecule and a supported lipid bilayer.[26] Therefore, the nanoscale topographic "movie" of the nanomaterial-related processes can be obtained by in situ AFM. (v): As described in this review, AFM can measure physical properties such as surface conductivity, static charge distribution, and magnetic force fields. (vi): AFM can be easily combined with other surface microscopic or spectroscopic technologies to provide complementary analysis for nanomaterials research because AFM has a relatively bigger imaging room compared with TEM and SEM. It should be noted that the application of AFM imaging for nanomaterials has several disadvantages: (i) The poor temporal resolution (in minute range) of normal AFM greatly limits their application in nanomaterials research. To overcome such limitation, scientists have already developed high-speed AFM [230-231] and large-scan area high-speed AFM [232-234], which increases the temporal resolution to milliseconds. (ii) The nanofilm (e.g. supported lipid bilayers) properties such as elasticity, fluidity, and diffusion may be affected by the solid support under nanofilms.[235] A support with well-defined nanopores is possible to overcome this limit by free-standing lipid bilayer.[236-238] (iii) Sample height compression effect may occur due to the elastic deformation of the sample and tip-broadening effect may occur due to the tip-sample convolution.[27-29] By choosing the appropriate probe and adjusting the

RSC Advances Accepted Manuscript

operation parameters, the artifacts can be minimized. (iv) Under liquid, the measured height of nanomaterials by AFM is dependent on the true nanomaterial height, the electrostatic interactions, and the applied force.[239-240] To measure the true topography of soft nanomaterials, it is important to eliminate the possible electrostatic repulsion and decrease the sample compression force.

Acknowledgments:

This work has been supported by research grants from the National Natural Science Foundation of China (51203024), the Shanghai Pujiang Talent Program (12PJ1430300), and the Special Fund for Talents in Minhang District of Shanghai (2012).

REFERENCES

1. G. Binnig, C. F. Quate, and C. Gerber, *Phys. Rev. Lett.*, 1986, **56**, 930-933.
2. T. Kajiyama, K. Tanaka, S.-R. Ge, and A. Takahara, *Prog. Surf. Sci.*, 1996, **52**, 1-52.
3. L. Bozec, and M. Horton, *Biophys. J.*, 2005, **88**, 4223-4231.
4. D. J. Müller, and Y. F. Dufrene, *Nat. Nano.*, 2008, **3**, 261-269.
5. A. A. Tseng, *Nano Today*, 2011, **6**, 493-509.
6. G. R. Luis, and L. Jian, *J. Phys.: Cond. Matter*, 2009, **21**, 483001.
7. D. L. Schodek, P. Ferreira, and M. F. Ashby, *Nanomaterials, nanotechnologies and design: an introduction for engineers and architects*. Butterworth-Heinemann: 2009.
8. M. J. Pitkethly, *Mater. Today*, 2004, **7**, 20-29.
9. N. Tran, and P. A. Tran, *ChemPhysChem*, 2012, **13**, 2481-2494.
10. G. Cao, and C. J. Brinker, *Annual Review of Nano Research: Volume 2*. World Scientific: 2008; Vol. 2.
11. D. Shi, *Nanomaterials and Devices*. Elsevier: 2014.
12. L. Yang, L. Zhang, and T. J. Webster, *Adv. Eng. Mater.*, 2011, **13**, B197-B217.
13. A. Gasparotto, D. Barreca, C. Maccato, and E. Tondello, *Nanoscale*, 2012, **4**, 2813-2825.
14. H. Dong, and W. Hu, Organic Nanomaterials. In *Springer Handbook of Nanomaterials*, Vajtai, R., Ed. Springer Berlin Heidelberg: 2013; pp 905-940.
15. A. C. Grimsdale, and K. Müllen, *Angew. Chem., Int. Ed.*, 2005, **44**, 5592-5629.
16. S.-F. Torabi, and Y. Lu, *Curr. Opin. Biotechnol.*, 2014, **28**, 88-95.
17. J. Yan, C. Hu, X. Liu, J. Zhong, G. Sun, and D. He, *Curr. Pharm. Des.*, 2015, **21**, 3181-3190.
18. C. Sanchez, P. Belleville, M. Popall, and L. Nicole, *Chem. Soc. Rev.*, 2011, **40**, 696-753.
19. S. J. Klaine, P. J. Alvarez, G. E. Batley, T. F. Fernandes, R. D. Handy, D. Y. Lyon, S. Mahendra, M. J. McLaughlin, and J. R. Lead, *Environ. Toxicol. Chem.*, 2008, **27**, 1825-1851.

RSC Advances Accepted Manuscript

20. Q. Zhang, E. Uchaker, S. L. Candelaria, and G. Cao, *Chem. Soc. Rev.*, 2013, **42**, 3127-3171.
21. T. Dawson, *Color. Technol.*, 2008, **124**, 261-272.
22. V. Morris, *Trends Biotechnol.*, 2011, **29**, 509-516.
23. J. A. Barreto, W. O'Malley, M. Kubeil, B. Graham, H. Stephan, and L. Spiccia, *Adv. Mater.*, 2011, **23**, H18-H40.
24. J. A. Hubbell, and A. Chilkoti, *Science*, 2012, **337**, 303-305.
25. L. Zhang, and T. J. Webster, *Nano Today*, 2009, **4**, 66-80.
26. J. Zhong, *Integr. Biol.*, 2011, **3**, 632-644.
27. K. L. Westra, A. W. Mitchell, and D. J. Thomson, *Journal of Applied Physics*, 1993, **74**, 3608-3610.
28. M. N. Murray, H. G. Hansma, M. Bezanilla, T. Sano, D. F. Ogletree, W. Kolbe, C. L. Smith, C. R. Cantor, S. Spengler, and P. K. Hansma, *Proceedings of the National Academy of Sciences of the United States of America*, 1993, **90**, 3811-3814.
29. J. Yang, J. Mou, J. Y. Yuan, and Z. Shao, *Journal of Microscopy*, 1996, **182**, 106-113.
30. J. Villarrubia, *J. Res. Natl. Inst. Stand. Technol.*, 1997, **102**, 425-454.
31. E. E. Urena-Benavides, P. J. Brown, and C. L. Kitchens, *Langmuir*, 2010, **26**, 14263-14270.
32. M. Plodinec, M. Loparic, and U. Aebi, *Cold Spring Harb Protoc*, **2010**, pdb.top86.
33. S. S. Wong, J. D. Harper, P. T. Lansbury, and C. M. Lieber, *Journal of the American Chemical Society*, 1998, **120**, 603-604.
34. P. Samorì, A. Ebner, L. Wildling, R. Zhu, C. Rankl, T. Haselgrübler, P. Hinterdorfer, and H. Gruber, Functionalization of Probe Tips and Supports for Single-Molecule Recognition Force Microscopy. In *STM and AFM Studies on (Bio)molecular Systems: Unravelling the Nanoworld*, Springer Berlin / Heidelberg: 2008; Vol. 285, pp 29-76.
35. M. Plodinec, M. Loparic, and U. Aebi, *Cold Spring Harb Protoc*, **2010**, pdb.prot5502-.
36. VEECO A Practical Guide to Scanning Probe Microscopy. http://www.veeco.com/pdfs/library/SPM_Guide_0829_05_166.pdf.
37. D. Fotiadis, Y. Liang, S. Filipek, D. A. Saperstein, A. Engel, and K. Palczewski, *Nature*, 2003, **421**, 127-128.
38. W. W. Scott, and B. Bhushan, *Ultramicroscopy*, 2003, **97**, 151-169.
39. G. Meyer, and N. M. Amer, *Appl. Phys. Lett.*, 1990, **57**, 2089-2091.
40. M. Raşa, B. Kuipers, and A. Philipse, *J. Colloid Interface Sci.*, 2002, **250**, 303-315.
41. N. Chen, and B. Bhushan, *J. Microsc.*, 2005, **220**, 96-112.
42. T. Ishida, W. Mizutani, Y. Aya, H. Ogiso, S. Sasaki, and H. Tokumoto, *J. Phys. Chem. B*, 2002, **106**, 5886-5892.
43. P. Bridger, Z. Bandić, E. Piquette, and T. McGill, *Appl. Phys. Lett.*, 1999, **74**, 3522-3524.
44. J. Nichols, D. Gundlach, and T. Jackson, *Appl. Phys. Lett.*, 2003, **83**, 2366-2368.
45. G. Neubauer, A. Erickson, C. C. Williams, J. J. Kopanski, M. Rodgers, and D. Adderton, *J. Vac. Sci. Technol., B*, 1996, **14**, 426-432.
46. H. Yamada, Y. Hirata, and J. Miyake, *J. Vac. Sci. Technol., A*, 1995, **13**, 1742-1745.
47. G. Mills, H. Zhou, A. Midha, L. Donaldson, and J. Weaver, *Appl. Phys. Lett.*, 1998, **72**, 2900-2902.
48. P. Eyben, S. Denis, T. Clarysse, and W. Vandervorst, *Mat. Sci. Eng.: B*, 2003, **102**, 132-137.
49. M. Rief, F. Oesterhelt, B. Heymann, and H. E. Gaub, *Science*, 1997, **275**, 1295-1297.
50. F. Gaboriaud, B. S. Parcha, M. L. Gee, J. A. Holden, and R. A. Strugnell, *Colloids Surf., B*, 2008, **62**, 206-213.
51. C. A. Clifford, and M. P. Seah, *Appl. Surf. Sci.*, 2005, **252**, 1915-1933.

RSC Advances Accepted Manuscript

52. A. Gestos, P. G. Whitten, G. M. Spinks, and G. G. Wallace, *Polymer Testing*, 2013, **32**, 655-664.
53. S.-Y. Gu, Q.-L. Wu, J. Ren, and G. J. Vancso, *Macromol. Rapid Commun.*, 2005, **26**, 716-720.
54. Y. Yang, G. Wang, and X. Li, *Nano Lett.*, 2011, **11**, 2845-2848.
55. R. D. Piner, J. Zhu, F. Xu, S. Hong, and C. A. Mirkin, *Science (Washington, DC, U. S.)*, 1999, **283**, 661-663.
56. K. Salaita, Y. Wang, and C. A. Mirkin, *Nat. Nanotechnol.*, 2007, **2**, 145-155.
57. M. Liu, N. A. Amro, and G.-y. Liu, *Annu. Rev. Phys. Chem.*, 2008, **59**, 367-386.
58. S. Xu, and G.-y. Liu, *Langmuir*, 1997, **13**, 127-129.
59. A. G. Khurshudov, K. Kato, and H. Koide, *Tribol. Lett.*, 1996, **2**, 345-354.
60. Y. Li, B. W. Maynor, and J. Liu, *J. Am. Chem. Soc.*, 2001, **123**, 2105-2106.
61. L. G. Rosa, and J. Liang, *J. Phys.: Cond. Matter*, 2009, **21**, 483001.
62. F. J. Rubio ‐ Sierra, W. M. Heckl, and R. W. Stark, *Adv. Eng. Mater.*, 2005, **7**, 193-196.
63. D. M. Czajkowsky, L. Li, J. Sun, J. Hu, and Z. Shao, *ACS Nano*, 2011, **6**, 190-198.
64. H. Qian, D.-S. Guo, and Y. Liu, *Chem. Eur. J.*, 2012, **18**, 5087-5095.
65. H. Qian, D.-S. Guo, and Y. Liu, *Asian J. Org. Chem.*, 2012, **1**, 155-159.
66. L. Ke, S. C. Lai, H. Liu, C. K. N. Peh, B. Wang, and J. H. Teng, *ACS Appl. Mater. Interfaces*, 2012, **4**, 1247-1253.
67. R. B. Pernites, M. J. L. Felipe, E. L. Foster, and R. C. Advincula, *ACS Appl. Mater. Interfaces*, 2011, **3**, 817-827.
68. J. Bochmann, A. Vainsencher, D. D. Awschalom, and A. N. Cleland, *Nat. Phys.*, 2013, **9**, 712-716.
69. G. Liu, D. J. Eichelsdoerfer, B. Rasin, Y. Zhou, K. A. Brown, X. Liao, and C. A. Mirkin, *Proc. Nat. Acad. Sci. U. S. A.*, 2013, **110**, 887-891.
70. X. Xu, J. Melcher, S. Basak, R. Reifenberger, and A. Raman, *Phys. Rev. Lett.*, 2009, **102**, 060801.
71. X. Xu, C. Carrasco, P. J. de Pablo, J. Gomez-Herrero, and A. Raman, *Biophys. J.*, 2008, **95**, 2520-2528.
72. J. Zhong, M. Ma, W. Li, J. Zhou, Z. Yan, and D. He, *Biopolymers*, 2014, **101**, 1181-1192.
73. J. Zhong, W. Zheng, L. Huang, Y. Hong, L. Wang, Y. Qiu, and Y. Sha, *BBA - Biomembranes*, 2007, **1768**, 1420-1429.
74. J. Zhong, C. Yang, W. Zheng, L. Huang, Y. Hong, L. Wang, and Y. Sha, *Biophys. J.*, 2009, **96**, 4610-4621.
75. E. Martines, J. Zhong, J. Muzard, A. C. Lee, B. B. Akhremitchev, D. M. Suter, and G. U. Lee, *Biophys. J.*, 2012, **103**, 649-657.
76. B. Heymann, and H. Grubmüller, *Phys. Rev. Lett.*, 2000, **84**, 6126-6129.
77. F.-C. Zhang, F. Zhang, H.-N. Su, H. Li, Y. Zhang, and J. Hu, *ACS Nano*, 2010, **4**, 5791-5796.
78. M. Kim, C.-C. Wang, F. Benedetti, M. Rabbi, V. Bennett, and P. E. Marszalek, *Adv. Mater.*, 2011, **23**, 5684-5688.
79. K. C. Neuman, and A. Nagy, *Nat. Meth.*, 2008, **5**, 491-505.
80. Y. Zhang, X. Hu, J. Sun, Y. Shen, J. Hu, X. Xu, and Z. Shao, *Microsc. Res. Tech.*, 2011, **74**, 614-626.
81. C. Dong, M. L. Kashon, D. Lowry, J. S. Dordick, S. H. Reynolds, Y. Rojanasakul, L. M. Sargent, and C. Z. Dinu, *Adv. Healthcare Mater.*, 2013, **2**, 945-951.
82. C. Dong, R. Eldawud, L. M. Sargent, M. L. Kashon, D. Lowry, Y. Rojanasakul, and C. Z. Dinu, *Environ. Sci. Nano*, 2014, **1**, 595-603.

RSC Advances Accepted Manuscript

83. H. Zhou, Q. Xu, S. Li, Y. Zheng, X. Wu, C. Gu, Y. Chen, and J. Zhong, *RSC Adv.*, 2015, **5**, 91633-91639.
84. Q. Xu, Y. Wan, T. S. Hu, T. X. Liu, D. Tao, P. H. Niewiarowski, Y. Tian, Y. Liu, L. Dai, Y. Yang, and Z. Xia, *Nat. Commun.*, 2015, **6**.
85. Y. Yan, Z. Hu, X. Zhao, T. Sun, S. Dong, and X. Li, *Small*, 2010, **6**, 724-728.
86. J. Zhong, M. Ma, J. Zhou, D. Wei, Z. Yan, and D. He, *ACS Appl. Mater. Interfaces*, 2013, **5**, 737-746.
87. J. Zhong, G. Sun, and D. He, *Nanoscale*, 2014, **6**, 12217-12228.
88. Y. Zhou, Z. Xie, K. A. Brown, D. J. Park, X. Zhou, P.-C. Chen, M. Hirtz, Q.-Y. Lin, V. P. Dravid, G. C. Schatz, Z. Zheng, and C. A. Mirkin, *Small*, 2015, **11**, 913-918.
89. G. Liu, Y. Zhou, R. S. Banga, R. Boya, K. A. Brown, A. J. Chipre, S. T. Nguyen, and C. A. Mirkin, *Chem. Sci.*, 2013, **4**, 2093-2099.
90. J. Zhong, and D. He, *Sci. Rep.*, 2015, **5**, 12998.
91. M. S. Anderson, and W. T. Pike, *Rev. Sci. Instrum.*, 2002, **73**, 1198-1203.
92. S. Moreno Flores, and J. L. Toca-Herrera, *Nanoscale*, 2009, **1**, 40-49.
93. X. Chen, K. M. Shakesheff, M. C. Davies, J. Heller, C. J. Roberts, S. J. B. Tendler, and P. M. Williams, *J. Phys. Chem.*, 1995, **99**, 11537-11542.
94. P. Karageorgiev, H. Orendi, B. Stiller, and L. Brehmer, *Appl. Phys. Lett.*, 2001, **79**, 1730-1732.
95. F. Iwata, K. Saruta, and A. Sasaki, *Appl Phys A*, 1998, **66**, S463-S466.
96. P. Xiao, J. Gu, J. Chen, J. Zhang, R. Xing, Y. Han, J. Fu, W. Wang, and T. Chen, *Chem. Commun.*, 2014, **50**, 7103-7106.
97. I. Casuso, N. Kodera, C. Le Grimellec, T. Ando, and S. Scheuring, *Biophys. J.*, 2009, **97**, 1354-1361.
98. P. D. Bosshart, A. Engel, and D. Fotiadis, *Rhodopsin: Methods and Protocols*, 2015, 189-203.
99. H. M. Ehmann, T. Kellner, and O. Werzer, *CrystEngComm*, 2014, **16**, 4950-4954.
100. I. Kirrou, and M. Belhaq, *Nonlinear Dyn.*, 2015, 1-13.
101. N. Shamitko ‐ Klingensmith, and J. Legleiter, *Scanning*, 2015, **37**, 23-35.
102. J. Zhong, X. Liu, D. Wei, J. Yan, P. Wang, G. Sun, and D. He, *Int. J. Biol. Macromol.*, 2015, **76**, 195-202.
103. J. Zhong, W. Zheng, L. Huang, Y. Hong, L. Wang, Y. Qiu, and Y. Sha, *Biochim. Biophys. Acta (BBA)-Biomembr.*, 2007, **1768**, 1420-1429.
104. M. Ma, J. Zhong, W. Li, J. Zhou, Z. Yan, J. Ding, and D. He, *Soft Matter*, 2013, **9**, 11325-11333.
105. M. Bag, T. S. Gehan, L. A. Renna, D. D. Algaier, P. M. Lahti, and D. Venkataraman, *RSC Adv.*, 2014, **4**, 45325-45331.
106. N. Kemnade, C. J. Shearer, D. J. Dieterle, A. S. Cherevan, P. Gebhardt, G. Wilde, and D. Eder, *Nanoscale*, 2015, **7**, 3028-3034.
107. Z. Xu, S. Zhu, M. Wang, Y. Li, P. Shi, and X. Huang, *ACS Appl. Mater. Interfaces*, 2015, **7**, 1355-1363.
108. Z. Zhang, L. Zhang, W. Li, A. Yu, and P. Wu, *ACS Appl. Mater. Interfaces*, 2015, **7**, 10395-10400.
109. A. Qin, X. Li, X. Zhao, D. Liu, and C. He, *ACS Appl. Mater. Interfaces*, 2015, **7**, 8427-8436.
110. D. Dallaeva, Ş. Ţălu, S. Stach, P. Škarvada, P. Tománek, and L. Grmela, *Appl. Surf. Sci.*, 2014, **312**, 81-86.
111. Y. Zhao, X. Liu, D. Y. Lei, and Y. Chai, *Nanoscale*, 2014, **6**, 1311-1317.
112. J. Tian, C. Tu, Y. Liang, J. Zhou, and X. Ye, *J. Neurosci. Methods*, 2015, **253**, 151-160.

RSC Advances Accepted Manuscript

113. L. H. Li, T. Xing, Y. Chen, and R. Jones, *Adv. Mater. Interfaces*, 2014, **1**, n/a-n/a.
114. F. Stipić, G. Pletikapić, Ž. Jakšić, L. Frkanec, G. Zgrablić, P. Burić, and D. M. Lyons, *J. Phys. Chem. B*, 2015, **119**, 1259-1264.
115. S. Tammam, S. Mathur, and N. Afifi, *J. Biomed. Nanotechnol.*, 2012, **8**, 439-49.
116. N. Oddone, A. Zambrana, M. Tassano, W. Porcal, P. Cabral, and J. Benech, *J Nanopart Res*, 2013, **15**, 1-14.
117. L. Qin, W. Zhang, J. Lu, A. G. Stack, and L. Wang, *Environ. Sci. Technol.*, 2013, **47**, 13365-13374.
118. L. Wang, C. V. Putnis, E. Ruiz-Agudo, J. Hövelmann, and A. Putnis, *Environ. Sci. Technol.*, 2015, **49**, 4184-4192.
119. T. Gädt, F. H. Schacher, N. McGrath, M. A. Winnik, and I. Manners, *Macromolecules*, 2011, **44**, 3777-3786.
120. S. N. Magonov, V. Elings, and M. H. Whangbo, *Surf. Sci.*, 1997, **375**, L385-L391.
121. S. Strbac, M. Nenadovic, L. Rajakovic, and Z. Rakocevic, *Appl. Surf. Sci.*, 2010, **256**, 3895-3899.
122. M. Nenadović, J. Potočnik, M. Ristić, S. Štrbac, and Z. Rakočević, *Surf. Coat. Technol.*, 2012, **206**, 4242-4248.
123. M. Jung, and J.-W. Choi, *Ultramicroscopy*, 2010, **110**, 670-675.
124. H. L. Gao, X. W. Zhang, J. H. Meng, Z. G. Yin, L. Q. Zhang, J. L. Wu, and X. Liu, *Thin Solid Films*, 2015, **576**, 81-87.
125. J. Zhong, M. Ma, W. Li, J. Zhou, Z. Yan, J. Ding, and D. He, *Biopolymers*, 2014, **101**, 1181-1192.
126. Lateral Force Microscopy (LFM). In *Encyclopedia of Nanotechnology*, Bhushan, B., Ed. Springer Netherlands: 2012; pp 1192-1192.
127. R. Bennewitz, Friction Force Microscopy. In *Fundamentals of Friction and Wear on the Nanoscale*, Gnecco, E.; Meyer, E., Eds. Springer International Publishing: 2015; pp 3-16.
128. A. Schirmeisen, U. Schwarz, and H. Hölscher, Friction Force Microscopy. In *Encyclopedia of Nanotechnology*, Bhushan, B., Ed. Springer Netherlands: 2012; pp 884-892.
129. R. K. Pandey, and V. Lakshminarayanan, *Thin Solid Films*, 2014, **562**, 367-371.
130. A. Peled, and J. Weiss, *Construct. Build. Mater.*, 2011, **25**, 4299-4302.
131. A. Peled, J. Castro, and W. J. Weiss, *Cement Concrete Comp.*, 2013, **36**, 48-55.
132. C. M. Almeida, V. Carozo, R. Prioli, and C. A. Achete, *J. Appl. Phys.*, 2011, **110**, 086101.
133. Y.-C. Liao, H. Sun, and B. L. Weeks, *Scanning*, 2012, **34**, 200-205.
134. U. Hartmann, *Annu. Rev. Mater. Sci.*, 1999, **29**, 53-87.
135. H. Li, X. Qi, J. Wu, Z. Zeng, J. Wei, and H. Zhang, *ACS Nano*, 2013, **7**, 2842-2849.
136. G. Cordova, S. Attwood, R. Gaikwad, F. Gu, and Z. Leonenko, *Nano Biomed. Eng.*, 2014, **6**, 31-39.
137. L. Angeloni, D. Passeri, M. Reggente, M. Rossi, D. Mantovani, L. Lazzaro, F. Nepi, F. De Angelis, and M. Barteri In *Experimental issues in magnetic force microscopy of nanoparticles*, NANOFORUM 2014, AIP Publishing: 2015; p 020010.
138. S. Sievers, K.-F. Braun, D. Eberbeck, S. Gustafsson, E. Olsson, H. W. Schumacher, and U. Siegner, *Small*, 2012, **8**, 2675-2679.
139. M. Coïsson, G. Barrera, F. Celegato, E. Enrico, E. Olivetti, P. Tiberto, and F. Vinai, *J. Magn. Magn. Mater.*, 2015, **373**, 250-254.
140. M. R. Tabasum, F. Zighem, J. D. L. T. Medina, A. Encinas, L. Piraux, and B. Nysten, *Nanotechnology*, 2014, **25**, 245707.
141. M. Gavagnin, H. D. Wanzenboeck, D. Belic, M. M. Shawrav, A. Persson, K. Gunnarsson, P. Svedlindh, and E. Bertagnolli, *Phys. Status Solidi A*, 2014, **211**, 368-374.

RSC Advances Accepted Manuscript

142. A. Fernández-Pacheco, R. Cowburn, L. Serrano-Ramón, M. R. Ibarra, and J. De Teresa, Combining Micromanipulation, Kerr Magnetometry and Magnetic Force Microscopy for Characterization of Three-Dimensional Magnetic Nanostructures. In *Surface Science Tools for Nanomaterials Characterization*, Kumar, C. S. S. R., Ed. Springer Berlin Heidelberg: 2015; pp 531-559.
143. C. Su, L. Huang, C. Prater, and B. Bhushan, Torsional Resonance Microscopy and Its Applications. In *Applied Scanning Probe Methods V*, Bhushan, B.; Kawata, S.; Fuchs, H., Eds. Springer Berlin Heidelberg: 2007; pp 113-148.
144. T. Kasai, B. Bhushan, L. Huang, and C. Su, *Nanotechnology*, 2004, **15**, 731-742.
145. C. Su, L. Huang, P. Neilson, and V. Kelley, *AIP Conf. Proc.*, 2003, **696**, 349-356.
146. T. Kunstmann, A. Schlarb, M. Fendrich, D. Paulkowski, T. Wagner, and R. Möller, *Appl. Phys. Lett.*, 2006, **88**.
147. I.-S. Hwang, C.-W. Yang, P.-H. Su, E.-T. Hwu, and H.-S. Liao, *Ultramicroscopy*, 2013, **135**, 121-125.
148. A. Yurtsever, A. M. Gigler, and R. W. Stark, *Ultramicroscopy*, 2009, **109**, 275-279.
149. G. WeissmÜLler, A. Yurtsever, L. T. Costa, A. B. F. Pacheco, P. M. Bisch, W. M. Heckl, and R. W. Stark, *Nano*, 2008, **03**.
150. A. Yurtsever, A. M. Gigler, C. Dietz, and R. W. Stark, *Appl. Phys. Lett.*, 2008, **92**.
151. Y. Chih-Wen, D. Ren-Feng, L. Shih-Hsiu, L. Hsien-Shun, L. Wei-Chiao, H. Kuang-Yuh, C. Chia-Seng, and H. Ing-Shouh, *Nanotechnology*, 2013, **24**, 305702.
152. A. Kaidatzis, and J. García-Martín, *Nanotechnology*, 2013, **24**, 165704.
153. C. Teichert, and I. Beinik, Conductive atomic-force microscopy investigation of nanostructures in microelectronics. In *Scanning Probe Microscopy in Nanoscience and Nanotechnology 2*, Springer: 2011; pp 691-721.
154. C. J. Chen, *Introduction to scanning tunneling microscopy*. Oxford University Press: 2008.
155. C. Li, Y. Bando, and D. Golberg, *ACS Nano*, 2010, **4**, 2422-2428.
156. P. Gundersen, K. O. Kongshaug, E. Selvig, and R. Haakenaasen, *J. Appl. Phys.*, 2010, **108**, 4308-114308.
157. J. Alvarez, I. Ngo, M.-E. Gueunier-Farret, J.-P. Kleider, L. Yu, P. Cabarrocas, S. Perraud, E. Rouvière, C. Celle, C. Mouchet, and J.-P. Simonato, *Nanoscale Res Lett*, 2011, **6**, 1-9.
158. K. Ganesan, S. Ilango, S. Mariyappan, M. F. Baroughi, M. Kamruddin, and A. K. Tyagi, *Appl. Phys. Lett.*, 2011, **98**, 092902.
159. S. Wang, G. Cheng, K. Cheng, X. Jiang, and Z. Du, *Nanoscale Res Lett*, 2011, **6**, 541.
160. Y. Lv, J. Cui, Z. M. Jiang, and X. J. Yang, *Nanotechnology*, 2013, **24**, 065702.
161. A. Vetushka, T. Itoh, Y. Nakanishi, A. Fejfar, S. Nonomura, M. Ledinský, and J. Kočka, *J. Non-Cryst. Solids*, 2012, **358**, 2545-2547.
162. I. Beinik, M. Kratzer, A. Wachauer, L. Wang, R. T. Lechner, C. Teichert, C. Motz, W. Anwand, G. Brauer, X. Y. Chen, X. Y. Hsu, and A. B. Djurišić, *J. Appl. Phys.*, 2011, **110**, 052005.
163. S. Raccosta, C. Baldacchini, A. Rita Bizzarri, and S. Cannistraro, *Appl. Phys. Lett.*, 2013, **102**, 203704.
164. F. Giannazzo, I. Deretzis, G. Nicotra, G. Fisichella, C. Spinella, F. Roccaforte, and A. La Magna, *Appl. Surf. Sci.*, 2014, **291**, 53-57.
165. M. Basletic, J. L. Maurice, C. Carretero, G. Herranz, O. Copie, M. Bibes, E. Jacquet, K. Bouzehouane, S. Fusil, and A. Barthelemy, *Nat. Mater.*, 2008, **7**, 621-625.
166. O. Yuki, K. Shigeru, O. Yutaka, and M. Takashi, *Nanotechnology*, 2011, **22**, 195202.
167. T. Massoud, V. Maurice, L. H. Klein, A. Seyeux, and P. Marcus, *Corr. Sci.*, 2014, **84**, 198-203.

RSC Advances Accepted Manuscript

168. G. A. MacDonald, P. A. Veneman, D. Placencia, and N. R. Armstrong, *ACS Nano*, 2012, **6**, 9623-9636.
169. S. Sonde, F. Giannazzo, V. Raineri, R. Yakimova, J.-R. Huntzinger, A. Tiberj, and J. Camassel, *Phys. Rev. B*, 2009, **80**, 241406.
170. S. Sonde, F. Giannazzo, V. Raineri, and E. Rimini, *Phys. Status Solidi B*, 2010, **247**, 912-915.
171. D. Wood, I. Hancox, T. S. Jones, and N. R. Wilson, *J. Phys. Chem. C*, 2015.
172. D. Sarid, *Scanning force microscopy: with applications to electric, magnetic, and atomic forces*. Oxford University Press: 1994.
173. R. Gaikwad, A. Hande, S. Das, S. K. Mitra, and T. Thundat, *Langmuir*, 2015, **31**, 679-684.
174. Q. Iqbal, P. Bernstein, Y. Zhu, J. Rahamim, P. Cebe, and C. Staii, *Nanotechnology*, 2015, **26**, 105702.
175. H. Du, D. Li, Y. Wang, C. Wang, D. Zhang, Y.-l. Yang, and C. Wang, *J. Phys. Chem. B*, 2013, **117**, 9895-9899.
176. S. E. Yalcin, C. Galande, R. Kappera, H. Yamaguchi, U. Martinez, K. A. Velizhanin, S. K. Doorn, A. M. Dattelbaum, M. Chhowalla, P. M. Ajayan, G. Gupta, and A. D. Mohite, *ACS Nano*, 2015, **9**, 2981-2988.
177. Q. Chen, L. Mao, Y. Li, T. Kong, N. Wu, C. Ma, S. Bai, Y. Jin, D. Wu, W. Lu, B. Wang, and L. Chen, *Nat. Commun.*, 2015, **6**.
178. H. R. Moutinho, R. G. Dhere, C.-S. Jiang, Y. Yan, D. S. Albin, and M. M. Al-Jassim, *J. Appl. Phys.*, 2010, **108**, 074503.
179. Y. Hu, N. Berdunov, C.-a. Di, I. Nandhakumar, F. Zhang, X. Gao, D. Zhu, and H. Sirringhaus, *ACS Nano*, 2014, **8**, 6778-6787.
180. L. C. Teague, O. D. Jurchescu, C. A. Richter, S. Subramanian, J. E. Anthony, T. N. Jackson, D. J. Gundlach, and J. G. Kushmerick, *Appl. Phys. Lett.*, 2010, **96**, 203305.
181. R. E. Hill-Pearce, V. Eless, A. Lartsev, N. A. Martin, I. L. Barker Snook, J. J. Helmore, R. Yakimova, J. C. Gallop, and L. Hao, *Carbon*, 2015, **93**, 896-902.
182. M. Salvador, S. M. Vorpahl, H. Xin, W. Williamson, G. Z. Shao, D. U. Karatay, H. W. Hillhouse, and D. S. Ginger, *Nano Lett.*, 2014, **14**, 6926-6930.
183. Y. Batra, D. Rai, and B. R. Mehta, *Appl. Phys. Express*, 2013, **6**.
184. H. Yoo, C. Bae, Y. Yang, S. Lee, M. Kim, H. Kim, Y. Kim, and H. Shin, *Nano Lett.*, 2014, **14**, 4413-4417.
185. A. Kumar, A. S. Patel, and T. Mohanty, *J. Phys. Chem. C*, 2012, **116**, 20404-20408.
186. Z. Z. Wang, Y. S. Gu, J. J. Qi, S. N. Lu, P. F. Li, P. Lin, and Y. Zhang, *RSC Adv.*, 2015, **5**, 42075-42080.
187. J. Li, X. Qi, G. L. Hao, K. Huang, and J. X. Zhong, *Fuller. Nanotub. Car. N.*, 2015, **23**, 777-781.
188. T. Wagner, D. Kohler, P. Milde, and L. M. Eng, *Appl. Phys. Lett.*, 2013, **103**.
189. G. J. Jones, A. Kazemi, S. Crampin, M. Phillips, and A. Ilie, *Appl. Phys. Express*, 2012, **5**.
190. Y. Li, C.-Y. Xu, and L. Zhen, *Appl. Phys. Lett.*, 2013, **102**.
191. C. V. Ben, H. D. Cho, T. W. Kang, and W. Yang, *Surf. Interface Anal.*, 2012, **44**, 755-758.
192. J. R. Matey, and J. Blanc, *J. Appl. Phys.*, 1985, **57**, 1437-1444.
193. E. Bussmann, M. Rudolph, G. S. Subramania, S. Misra, S. M. Carr, E. Langlois, J. Dominguez, T. Pluym, M. P. Lilly, and M. S. Carroll, *Nanotechnology*, 2015, **26**, 085701.
194. F. Bassani, P. Periwal, B. Salem, N. Chevalier, D. Mariolle, G. Audoit, P. Gentile, and T. Baron, *Phys. Status Solidi-R.*, 2014, **8**, 312-316.
195. P. Periwal, F. Bassani, G. Patriarche, L. Latu-Romain, V. Brouzet, B. Salem, and T. Baron, *Phys. Status Solidi A*, 2014, **211**, 509-513.

RSC Advances Accepted Manuscript

196. I. Humer, O. Bethge, M. Bodnarchuk, M. Kovalenko, M. Yarema, W. Heiss, H. P. Huber, M. Hochleitner, P. Hinterdorfer, F. Kienberger, and J. Smoliner, *J. Appl. Phys.*, 2011, **109**.
197. K. W. Park, H. P. Nair, A. M. Crook, S. R. Bank, and E. T. Yu, *Appl. Phys. Lett.*, 2011, **99**.
198. Z. Lin, G. Bremond, and F. Bassani, *Nanoscale Research Lett.*, 2011, **6**, 163.
199. P. Eyben, T. Janssens, and W. Vandervorst, *Mater. Sci. Eng.: B*, 2005, **124–125**, 45-53.
200. A. Schulze, T. Hantschel, P. Eyben, A. S. Verhulst, R. Rooyackers, A. Vandooren, J. Mody, A. Nazir, D. Leonelli, and W. Vandervorst, *Nanotechnology*, 2011, **22**, 185701.
201. P. Eyben, T. Clarysse, J. Mody, A. Nazir, A. Schulze, T. Hantschel, and W. Vandervorst, *Solid-State Electron.*, 2012, **71**, 69-73.
202. S. Tewfik, S. Marco, and C. Matteo, *Nanotechnology*, 2012, **23**, 405704.
203. P. Calka, E. Martinez, V. Delaye, D. Lafond, G. Audoit, D. Mariolle, N. Chevalier, H. Grampeix, C. Cagli, V. Jousseaume, and C. Guedj, *Nanotechnology*, 2013, **24**, 085706.
204. A. Schulze, T. Hantschel, P. Eyben, A. S. Verhulst, R. Rooyackers, A. Vandooren, and W. Vandervorst, *Ultramicroscopy*, 2013, **125**, 18-23.
205. S. Doering, A. Wachowiak, M. Rochel, C. Nowak, M. Hoffmann, U. Winkler, M. Richter, H. Roetz, S. Eckl, and T. Mikolajick, *Microelectron. Eng.*, 2015, **142**, 40-46.
206. I. S. Fraser, R. A. Oliver, J. Sumner, C. McAleese, M. J. Kappers, and C. J. Humphreys, *Appl. Surf. Sci.*, 2007, **253**, 3937-3944.
207. J. Liu, K. C. Mandal, and G. Koley, *Semicond. Sci. Technol.*, 2009, **24**, 045012.
208. M. Truchlý, T. Plecenik, O. Krško, M. Gregor, L. Satrapinskyy, T. Roch, B. Grančič, M. Mikula, A. Dujavová, Š. Chromik, P. Kúš, and A. Plecenik, *Physica C*, 2012, **483**, 61-66.
209. M. Radmacher, R. Tillmann, and H. Gaub, *Biophys. J.*, 1993, **64**, 735.
210. I. S. Gilmore, M. P. Seah, and J. E. Johnstone, *Surf. Interface Anal.*, 2003, **35**, 888-896.
211. A. C. Hellgren, *Prog. Org. Coat.*, 1998, **34**, 91-99.
212. Y. Hirayama, T. Sogawa, K. Suzuki, K. Kanisawa, and H. Yamaguchi, *Phys. Status Solidi B*, 2007, **244**, 2988-3001.
213. K. Kimura, K. Kobayashi, H. Yamada, and K. Matsushige, *Nanotechnology*, 2008, **19**, 065701.
214. F. Zhao, Y. Huang, L. Liu, Y. Bai, and L. Xu, *Carbon*, 2011, **49**, 2624-2632.
215. A. Majumdar, *Annu. Rev. Mater. Sci.*, 1999, **29**, 505-585.
216. B. Cretin, S. Gomes, N. Trannoy, and P. Vairac, Scanning thermal microscopy. In *Microscale and nanoscale heat transfer*, Springer: 2007; pp 181-238.
217. E. Puyoo, S. Grauby, J.-M. Rampnoux, E. Rouvière, and S. Dilhaire, *J. Appl. Phys.*, 2011, **109**, 024302.
218. S. p. Grauby, E. Puyoo, J.-M. Rampnoux, E. Rouvière, and S. Dilhaire, *The Journal of Physical Chemistry C*, 2013, **117**, 9025-9034.
219. K. Yoon, G. Hwang, J. Chung, H. g. Kim, O. Kwon, K. D. Kihm, and J. S. Lee, *Carbon*, 2014, **76**, 77-83.
220. J. Chung, K. Kim, G. Hwang, O. Kwon, S. Jung, J. Lee, J. W. Lee, and G. T. Kim, *Rev. Sci. Instrum.*, 2010, **81**, 114901.
221. A. Kaźmierczak-Bałata, J. Bodzenta, M. Krzywiecki, J. Juszczyk, J. Szmidt, and P. Firek, *Thin Solid Films*, 2013, **545**, 217-221.
222. S. Kar-Narayan, S. Crossley, X. Moya, V. Kovacova, J. Abergel, A. Bontempi, N. Baier, E. Defay, and N. D. Mathur, *Appl. Phys. Lett.*, 2013, **102**, 032903.
223. M. Sadhukhan, T. Bhowmik, M. K. Kundu, and S. Barman, *RSC Adv.*, 2014, **4**, 4998-5005.
224. S. H. Kim, W. Song, M. W. Jung, M. A. Kang, K. Kim, S. J. Chang, S. S. Lee, J. Lim, J. Hwang, and S. Myung, *Adv. Mater.*, 2014, **26**, 4247-4252.
225. J. Zhong, and D. He, *Chem. Eur. J.*, 2012, **18**, 4148-4155.

RSC Advances Accepted Manuscript

226. J. R. Harris, and S. De Carlo, Negative Staining and Cryo-negative Staining: Applications in Biology and Medicine. In *Electron Microscopy*, Springer: 2014; pp 215-258.
227. C. Lambare, P. Y. Tessier, F. Poncin-Epaillard, and D. Debarnot, *RSC Adv.*, 2015, **5**, 62348-62357.
228. Y. Shan, and H. Wang, *Chem. Soc. Rev.*, 2015, **44**, 3617-3638.
229. N. Matsko, and V. Mittal, *Soft matter*, 2014, **10**, 5478-5488.
230. T. Ando, T. Uchihashi, N. Kodera, D. Yamamoto, A. Miyagi, M. Taniguchi, and H. Yamashita, *Pflugers Arch.*, 2008, **456**, 211-225.
231. P. K. Hansma, G. Schitter, G. E. Fantner, and C. Prater, *Science*, 2006, **314**, 601-602.
232. D. M. Carberry, L. Picco, P. G. Dunton, and M. J. Miles, *Nanotechnology*, 2009, **20**.
233. B. Zhao, J. P. Howard-Knight, A. D. L. Humphris, L. Kailas, E. C. Ratcliffe, S. J. Foster, and J. K. Hobbs, *Rev. Sci. Instrum.*, 2009, **80**.
234. G. E. Fantner, R. J. Barbero, D. S. Gray, and A. M. Belcher, *Nat. Nano.*, 2010, **5**, 280-285.
235. K. El Kirat, S. Morandat, and Y. F. Dufrene, *BBA - Biomembranes*, 2010, **1798**, 750-765.
236. I. Mey, M. Stephan, E. K. Schmitt, M. M. Muller, M. Ben Amar, C. Steinem, and A. Janshoff, *J. Am. Chem. Soc.*, 2009, **131**, 7031-7039.
237. C. Hennesthal, J. Drexler, and C. Steinem, *ChemPhysChem*, 2002, **3**, 885-889.
238. C. Hennesthal, and C. Steinem, *J. Am. Chem. Soc.*, 2000, **122**, 8085-8086.
239. J. Zhong, C. Yang, W. Zheng, L. Huang, Y. Hong, L. Wang, and Y. Sha, *Colloids Surf. B: Biointerfaces*, 2010, **77**, 40-46.
240. D. J. Müller, and A. Engel, *Biophys. J.*, 1997, **73**, 1633-1644.

RSC Advances Accepted Manuscript

Table 1. Comparison of three main operation modes of AFM. Reprinted with permission from reference [26]. (Copyright 2011 The Royal Society of Chemistry).

Operation mode	Probes	Cantilever	Tip-sample distance	Force	Advantages	Disadvantages
Contact mode	Silicon nitride probes	The cantilever is deflected: constant force; or constant height	Physical contact <0.5 nm	Repulsive 10^{-9}-10^{-6} N	High scan speeds Good for rough samples Used in friction analysis High resolution	Lateral (shear) forces may distort soft samples In ambient conditions, may get strong capillary force due to the adsorbed thin water layer
Non-contact mode	Silicon probes with high spring constant of 20-100 N/m	The cantilever is oscillated (amplitude < 10 nm)	Above the sample 1-10 nm	Attractive 10^{-12} N	Both normal and lateral forces are minimized; good for very soft samples Can get atomic resolution in a ultra high vacuum (UHV) environment Extended probe lifetime	Generally lower resolution In ambient conditions. adsorbed water lay may cause the tip "jump-to-contact" Imaging of liquid layer and not of the underlying surface in the presence of water Slower scan speed than tapping and contact modes Usually need UHV to have best imaging
Tapping Mode	Silicon probes with spring constant of 2-50 N/m	The cantilever is oscillated (amplitude > 20 nm)	Intermittent contact 0.5-2 nm	Both repulsive and attractive forces 10^{-12} N	Lateral forces almost eliminated Higher lateral resolution on most samples Lower forces; less damage to soft samples and tips Good for biological samples	Slower scan speed than in contact mode

RSC Advances Accepted Manuscript

Figure captions:

Figure 1. Schematic diagram of AFM components: probe, piezo scanner, feedback control system, and software. Adapted with permission from reference [26]. (Copyright 2011 The Royal Society of Chemistry).

Figure 2. Representative AFM height images of regenerated silk fibroin (2.4 μg/mL) after different incubation times. Adapted with permission from reference [104]. (Copyright 2011 The Royal Society of Chemistry).

Figure 3. AFM height images of Ag thin films with different root-mean-square roughness, ranging from 0.83 nm to 7.14 nm. Reprinted with permission from reference [111]. (Copyright 2014 The Royal Society of Chemistry).

Figure 4. AFM height image (A) and deflection image (B) of the same area of boron nitride nanosheet covered Cu foil after the heating at 250 ℃ in air for 2 h. Both the two images have the same scale bar. Adapted with permission from reference [113]. (Copyright 2014 Wiley-VCH Verlag 4148 GmbH&Co. KGaA).

Figure 5. Representative AFM height and phase images of regenerated SF self-assembly structures after different incubation times at a concentration of 0.006%. Incubation times, visual fields and height scales are shown at the upper right corner, the lower left corner and the lower right corner, respectively, of each image. (a–e) are zoomed-in height images from the corresponding regions shown in (A–E). (a', c', d', e') are the corresponding AFM phase images to AFM height images of (a, c, d, e). Phase scales are shown at the lower right corner of these phase images. White and black arrows except those in (5d') indicate RSF protofilaments and RSF protofibrils, respectively. White and black arrows in (d') indicated two types of cuboid-like protofibrils with different periodic intervals. (1–2) are section analyses along the corresponding white dashed lines in (5d'). Grey arrows indicate

RSC Advances Accepted Manuscript

membrane-like features. Reprinted with permission from reference [125]. (Copyright 2014 Wiley-VCH Verlag 4148 GmbH&Co. KGaA).

Figure 6. LSM images and corresponding height images of bare gold surface (a), thiocholesterol self-assembled monolayer on gold surface (b), β-cyclodextrin/thiocholesterol inclusion complex self-assembled monolayer on gold surface (c), and methyl-β-cyclodextrin/thiocholesterol inclusion complex self-assembled monolayer on gold surface (d). All the images are 10 μm × 10 μm and average roughness values (z scale) are 6.0 nm, 8.0 nm, 10.0 nm and 13.0 nm respectively for (a), (b), (c), and (d). Reprinted with permission from reference [129]. (Copyright 2014 Elsevier Ltd.).

Figure 7. AFM height image (A) and MFM images (B-G) of single-layer graphene on 90 nm SiO_2/Si at various lift heights: (B): 150, (C) 100, (D) 80, (E) 50, (F) 30, and (G) 25 nm. Inset in panel A: optical image of the single-layer graphene on 90 nm SiO_2/Si. (H) The plot of phase shift vs lift height obtained in the magnetic force microscopy measurements on single-layer graphene. Red curve is the exponentially fitted curve. Reprinted with permission from reference [135]. (Copyright 2014 American Chemical Society).

Figure 8. AFM images of the same area of duplex DNA on a mica surface in water taken with two different modes using the same AFM probe under the same environment. The scan area and the pixel size of all images are 800 nm × 800 nm and 256 × 256, respectively. The scan rate is 0.5 Hz. The imaging sequence is from (a) to (b). (a): non contact-torsional resonance mode with the free torsional oscillation amplitude ~ 0.8 nm, ft=140.35 kHz, $\triangle$ f=+20 Hz, Q factor ~ 70. The line profile along the dashed line is shown at the bottom. (b): non contact mode with the free flexural oscillation amplitude ~ 1.2 nm, f_f=35.35 KHz, $\triangle$

RSC Advances Accepted Manuscript

f=+40 Hz, Q factor ~ 5. The line profile along the dashed line is shown at the bottom. Reprinted with permission from reference [147]. (Copyright 2014 Elsevier Ltd.).

Figure 9. (a) Proposed band edge alignments for the ITO/CuPc/PtIr heterojunctions, assuming a pretreatment-dependent work function range for ITO of 4.2-5.2 eV (for DSC, AE-ITO, and OP-ITO), an IP/HOMO energy for CuPc of 4.8 eV, a LUMO of 3.2 eV, and a work function for the PtIr tip of 5.2 eV. (b) Schematic representation of the scanning current spectroscopy mapping experiment. Current-voltage (J-V) curves are collected from an array of spatially resolved points, with sampling dimensions of 500 $\times$ 500 nm and a point-to-point separation distance of 20 nm. The apparent hole mobility and the apparent power dependence of the current-voltage behavior were extracted from these individual J-V curves. A power dependence that deviates from 2 indicates the presence of a nonohmic contact between the bottom electrode and the organic semiconductor. Reprinted with permission from reference [168]. (Copyright 2012 American Chemical Society).

Figure 10. (a) AFM height image of asphaltene aggregates and (b) corresponding EFM image at a lift height of 35 nm. (c) and (d) provide the cross section of the height image and EFM image at athe same location corresponding to the white horizontal line shown in (a) and (b), respectively. Reprinted with permission from reference [173]. (Copyright 2015 American Chemical Society).

Figure 11. Cross-sectional images and depth profiles of a bulk heterojunction device. (a) height and (c) phase images of ITO/MoO_x/P3HT:PCBM/LiF/Al device cross-section obtained with AFM (scale bars, 200 nm). The line profiles in (b) and (d) correspond to the red lines in (a) and (c), respectively. Surface potential images of the P3HT:PCBM bulk heterojunction device in open-circuit (e) in the dark and (f) under AM 1.5G (100 mW/cm^2)

RSC Advances Accepted Manuscript

illumination (scale bar, 250 nm). (g) Surface potential depth profiles of the device in open-circuit in the dark (solid black squares), in open-circuit under AM 1.5G illumination (open black squares), in short-circuit in the dark (solid purple line) and in short-circuit under AM 1.5G illumination (open orange diamonds). (h) Surface potential depth profiles of the P3HT:PCBM bulk heterojunction device in the dark with bias voltages ranging from -1.0 to +1.0V. Reprinted with permission from reference [177]. (Copyright 2015 Macmillan Publishers Ltd.).

Figure 12. (a): Schematic of the SCM measurement. (b)–(e): AFM and SCM images of the buried single-electron transistor donor structure. (b): Contact mode AFM height image over the donor region showing the flat topography (1 nm roughness). (c): SCM amplitude ($\partial C/\partial V$) over the donor structure. Contrast is due to variations in the dopant density. (d): SCM phase signal. Contrast is due to variation of the dopant type. (e): SCM image of the active region of the donor device. Charging effects in the native oxide caused by the tip lead to nonuniform contrast over the donor doped regions. Reprinted with permission from reference [193]. (Copyright 2015 IOP Publishing Ltd.).

Figure 13. Typical (a) AFM height and (b) SSRM image (bias voltage 1.5 V) of the $YBa_2Cu_3O_{6+x}$ thin film surface stored in air for several days before the ion beam etching. Reprinted with permission from reference [208]. (Copyright 2012 Elsevier Ltd.).

Figure 14. The FMAFM images obtained from the cross-section of the composites reinforced by different carbon fibers. FMAFM image (a) and section analysis (b) of the interphase in traditional carbon fiber composites, FMAFM image (c) and section analysis (d) of the interphase in polyhedral oligo silsesquioxane and carbon nanotubes grafted

RSC Advances Accepted Manuscript

carbon fiber composites. Reprinted with permission from reference [214]. (Copyright 2011 Elsevier Ltd.).

Figure 15. Vapor-liquid-solid Si nanowires: (a) cross-section SEM image, (b) top view scanning electron microscopy image after the encapsulation process, (c) 2 μm × 3 μm AFM height image, and (d) 2 μm × 3 μm SThM image. Reprinted with permission from reference [218]. (Copyright 2013 American Chemical Society).

RSC Advances Accepted Manuscript

Figure 1

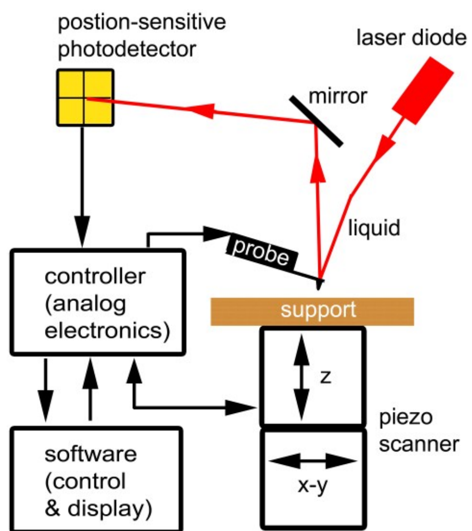

RSC Advances Accepted Manuscript

Figure 2

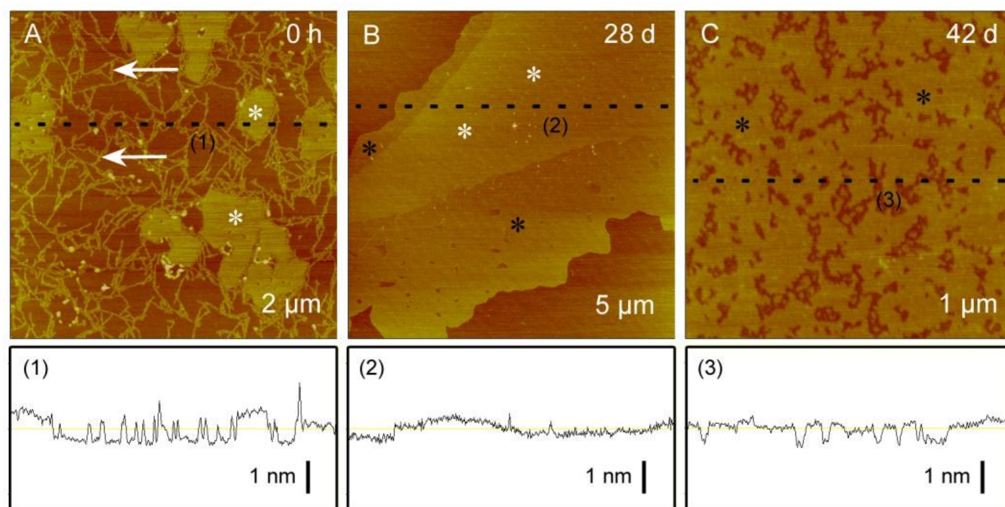

RSC Advances Accepted Manuscript

Figure 3

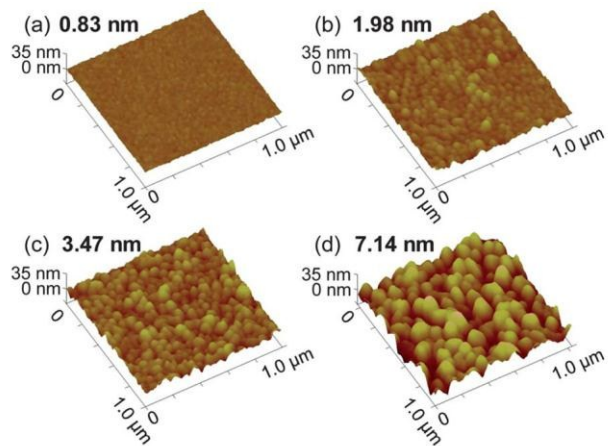

RSC Advances Accepted Manuscript

Figure 4

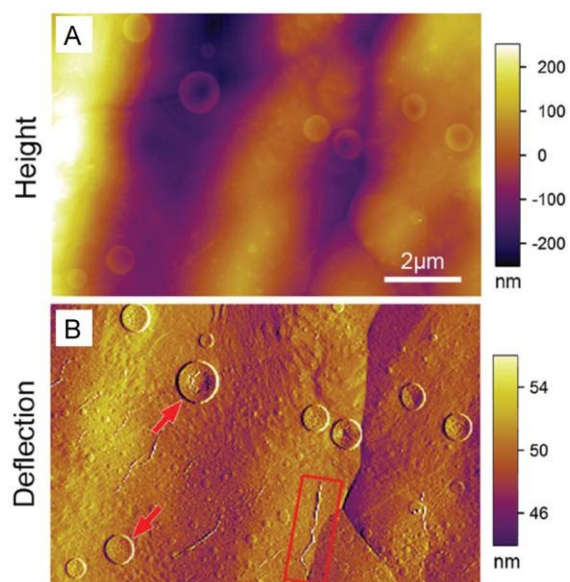

RSC Advances Accepted Manuscript

Figure 5

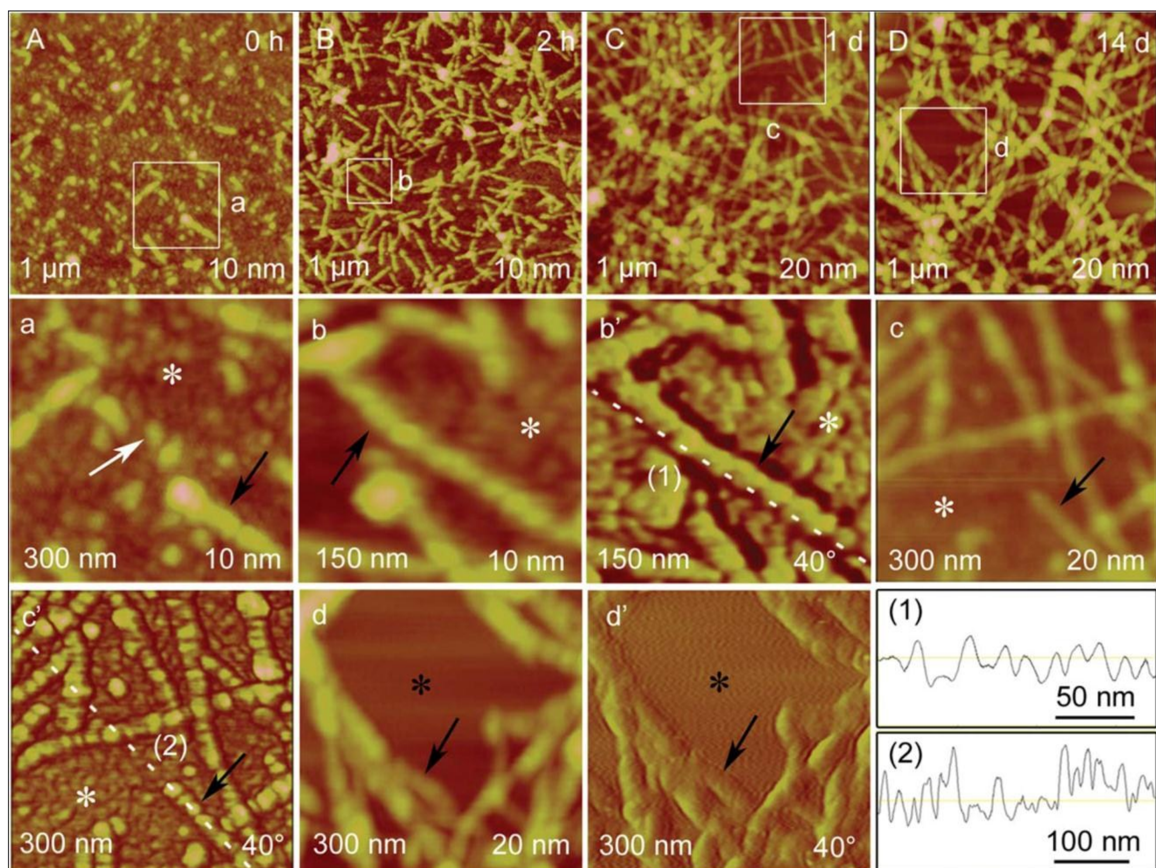

RSC Advances Accepted Manuscript

Figure 6

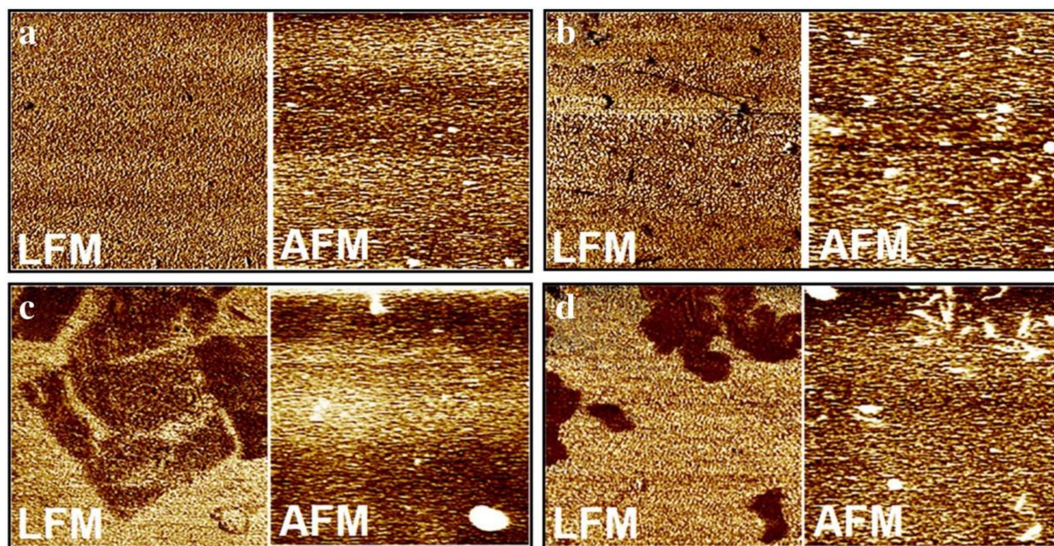

RSC Advances Accepted Manuscript

Figure 7

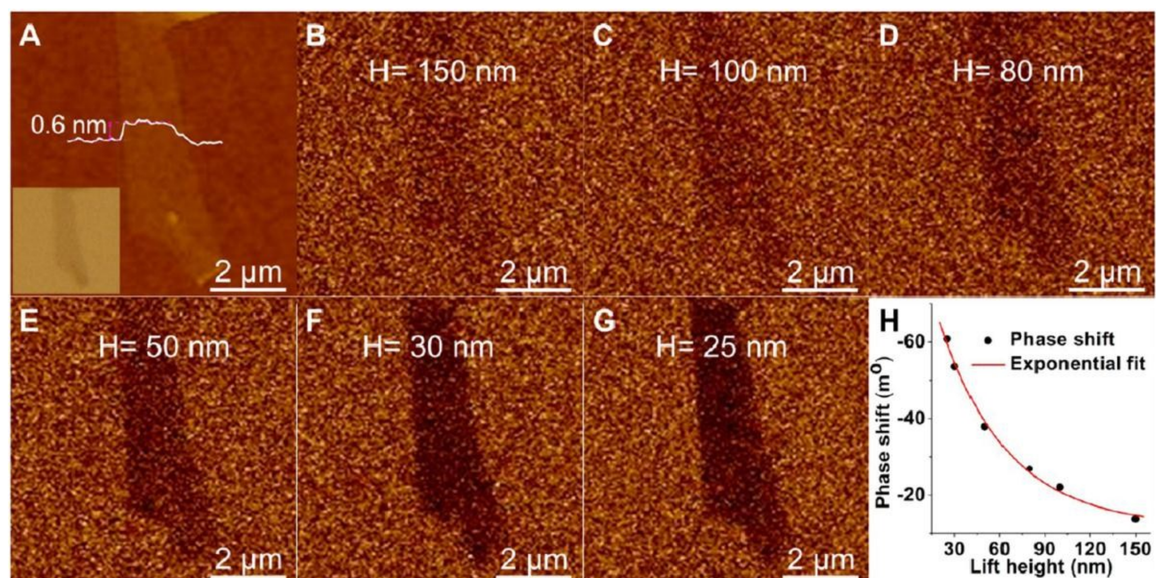

RSC Advances Accepted Manuscript

Figure 8

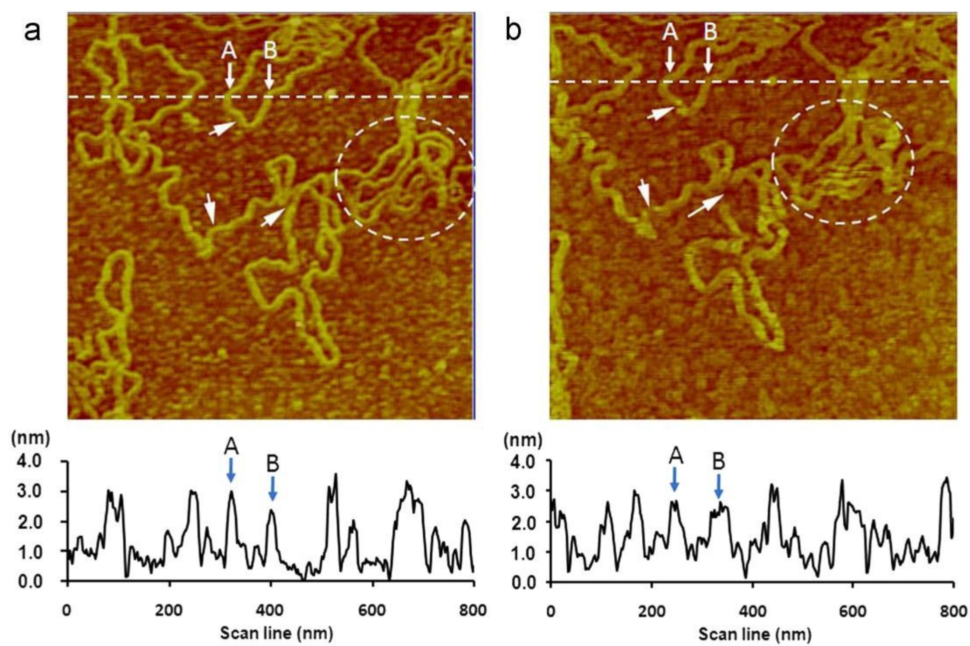

RSC Advances Accepted Manuscript

Figure 9

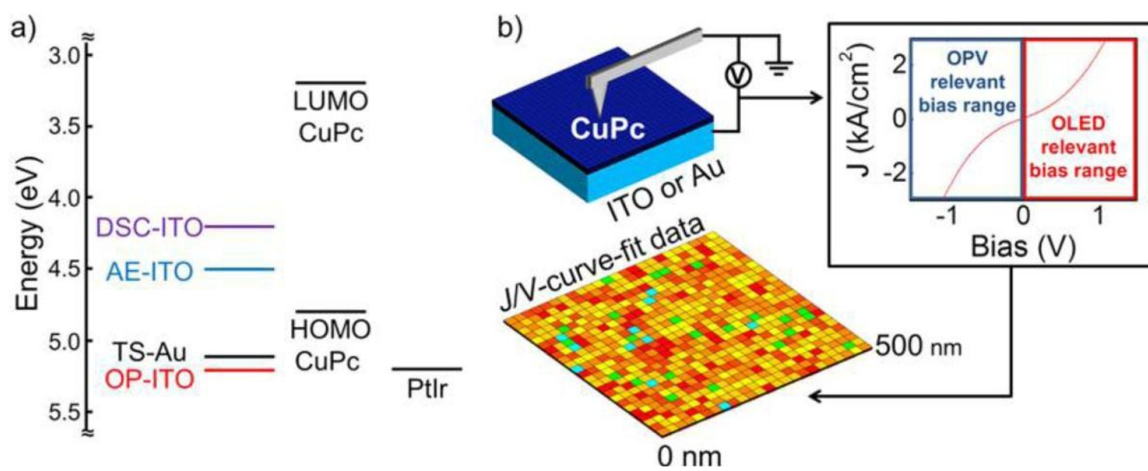

RSC Advances Accepted Manuscript

Figure 10

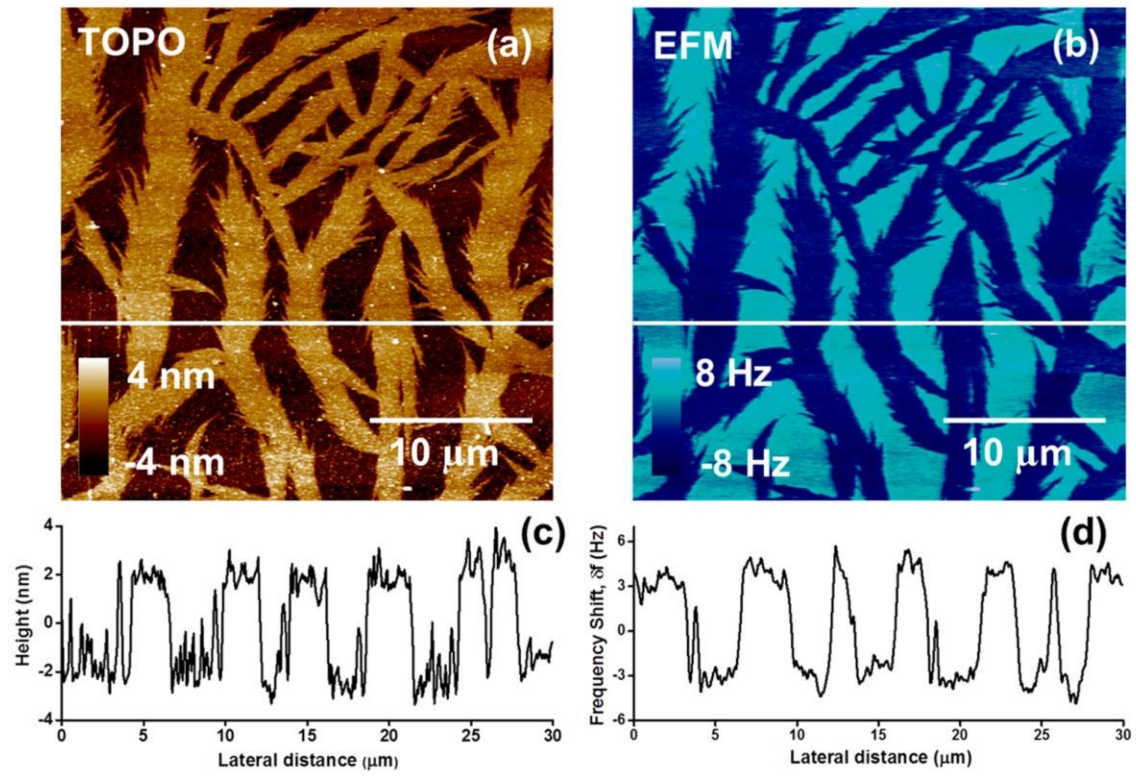

RSC Advances Accepted Manuscript

Figure 11

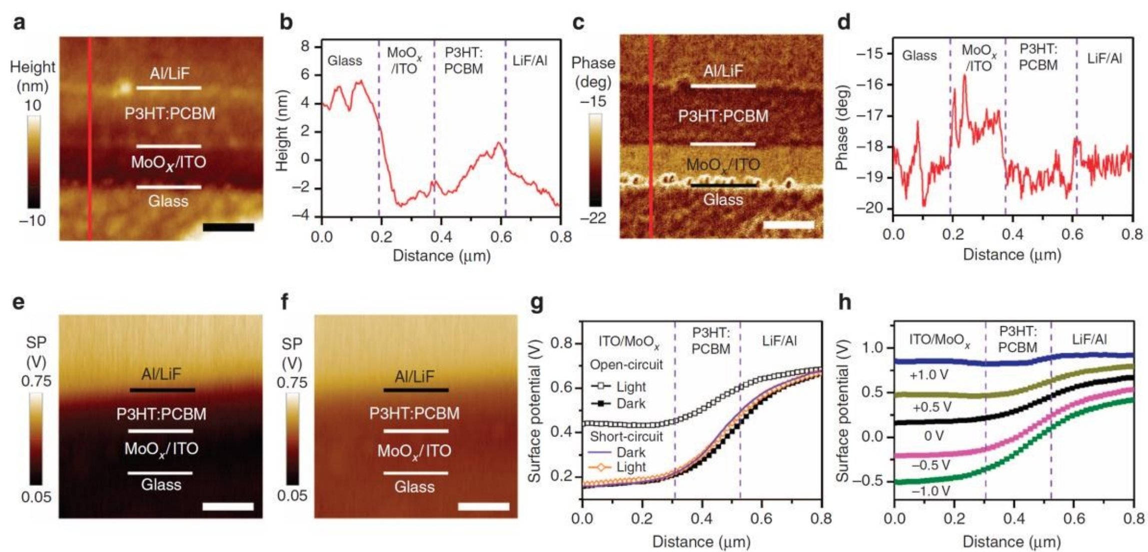

RSC Advances Accepted Manuscript

Figure 12

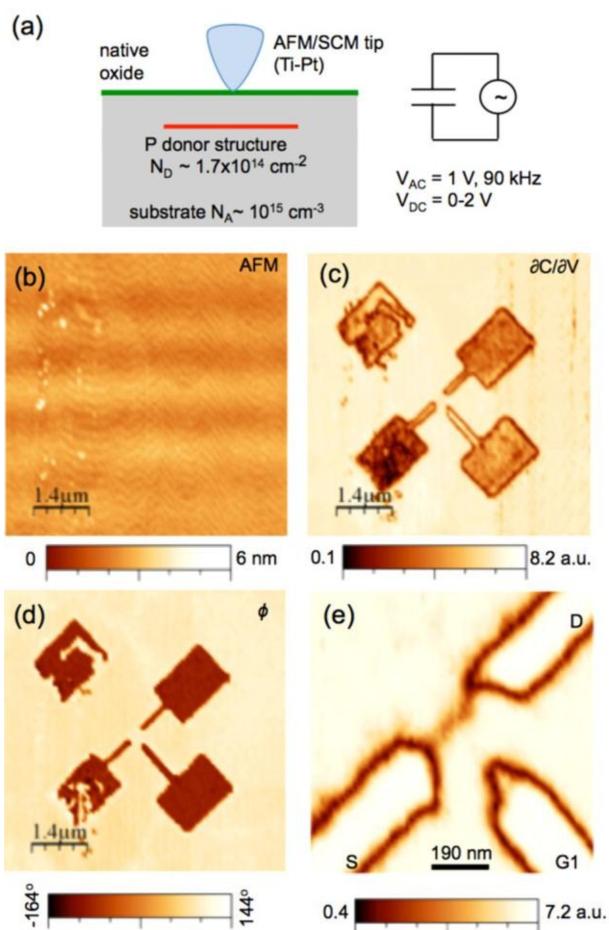

RSC Advances Accepted Manuscript

Figure 13

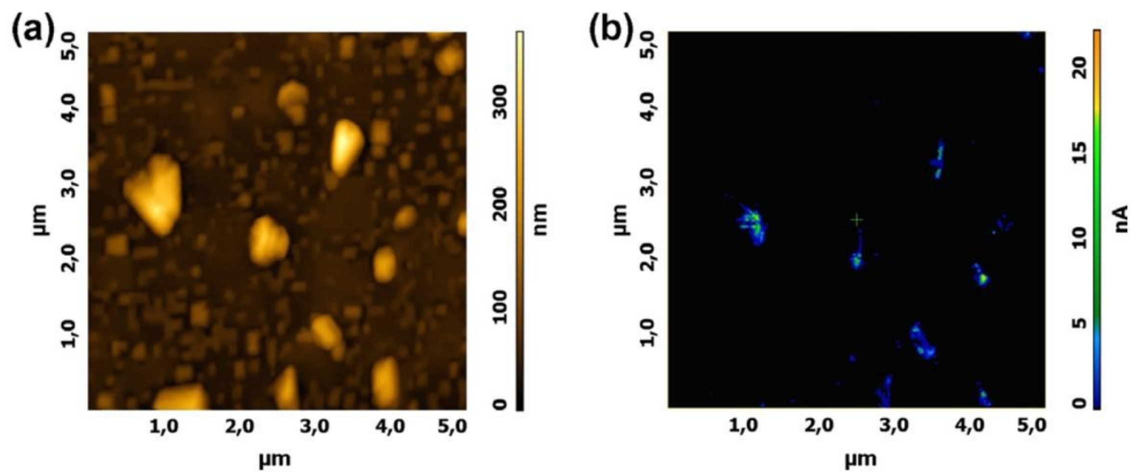

RSC Advances Accepted Manuscript

Figure 14

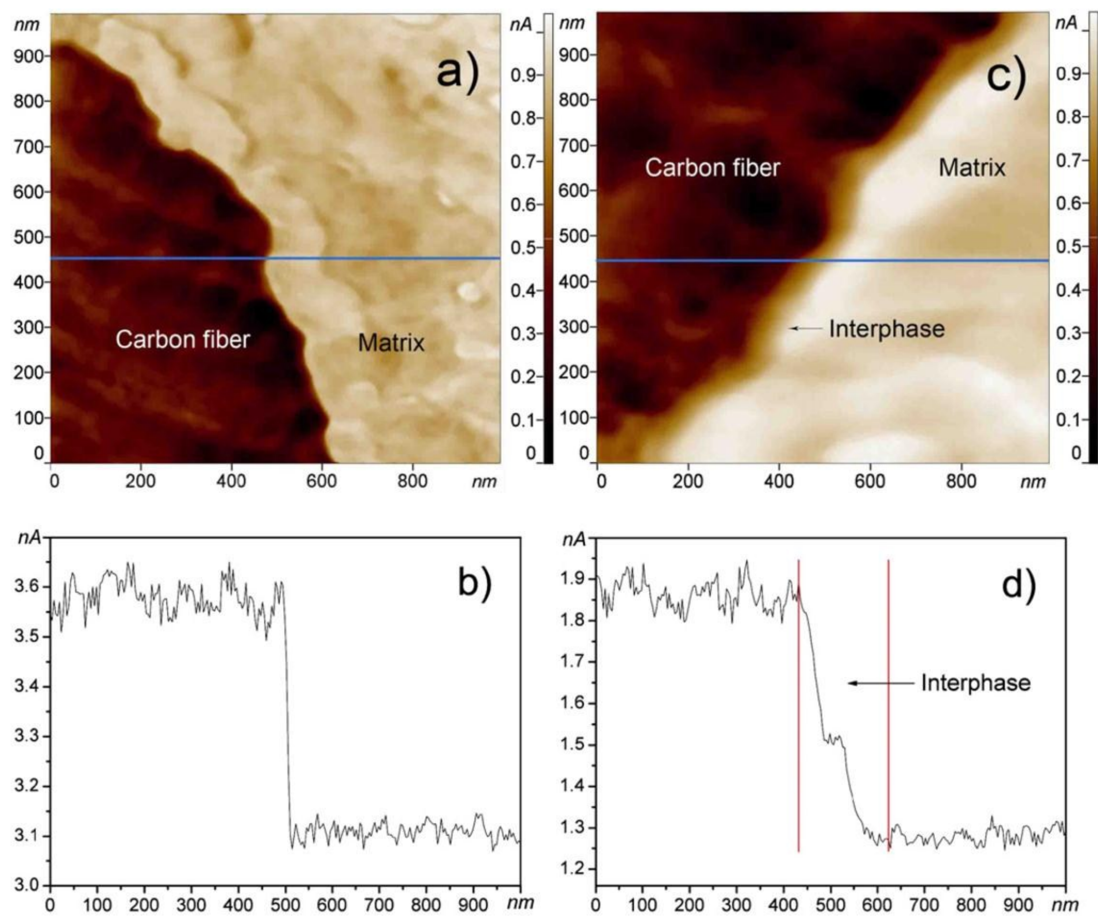

RSC Advances Accepted Manuscript

Figure 15

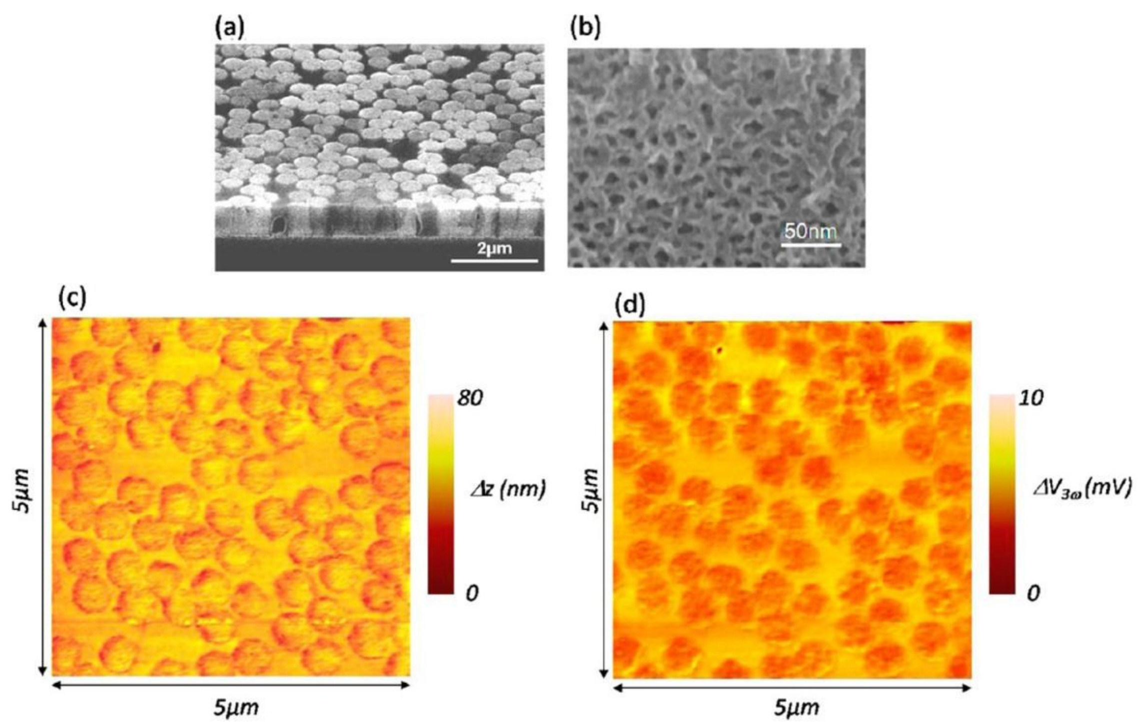

RSC Advances Accepted Manuscript

Graphical Abstract

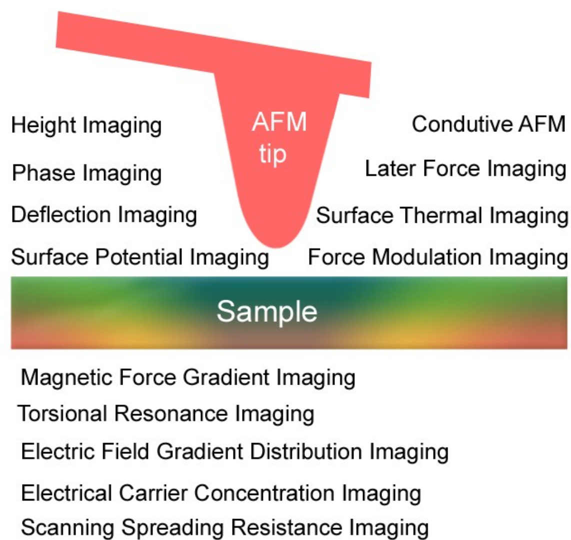

Atomic force microscopy can image the nanomaterial properties such as the topography, elasticity, adhesion, friction, electrical properties, and magnetism.

RSC Advances Accepted Manuscript